The Canadian Mineralogist
Vol. 59, pp. 1453-1484 (2021)
DOI: 10.3749/canmin.2100018

THE EFFECTS OF POST-CUMULUS ALTERATION ON THE DISTRIBUTION OF CHALCOPHILE ELEMENTS IN MAGMATIC SULFIDE DEPOSITS AND IMPLICATIONS FOR THE FORMATION OF LOW-S-HIGH-PGE ZONES: THE LUANGA DEPOSIT, CARAJÁS MINERAL PROVINCE, BRAZIL

EDUARDO MANSUR[§] AND SARAH-JANE BARNES

Sciences de la Terre, Université du Québec à Chicoutimi, Québec, G7H 2B1, Canada

CESAR F. FERREIRA FILHO

Instituto de Geociências, Universidade de Brasília, Brasília-DF 70910-900, Brazil

ABSTRACT

Most of the World's platinum-group element ore deposits occur as thin stratiform layers within layered intrusions. These layers generally contain disseminated base-metal sulfides or chromite. However, cryptic platinum-group element deposits also occur without chromite or base-metal sulfides in what are known as low-S-high platinum-group element deposits. The origin of these deposits is not clearly understood. The Luanga Complex hosts the largest platinum-group elements resource in South America (*i.e.*, 142 Mt at 1.24 ppm Pt + Pd + Au and 0.11% Ni) and hosts both a platinum-group element deposit containing disseminated base-metal sulfides (style 1) and a low-S-high platinum-group element deposit (style 2). It therefore offers the opportunity to compare the two deposit types in the same overall geological setting and consider how the low-S-high platinum-group element deposit could have formed. The first deposit style is termed the Sulfide zone and consists of a 10–50 meter-thick interval with disseminated base metal sulfides, whereas the second style is named low-S-high-Pt-Pd zone and consists of 2–10 meter-thick discontinuous lenses of 1–5 meter-thick sulfide- and oxide-free harzburgite and orthopyroxenite with discrete platinum-group minerals. Secondary assemblages commonly replace primary igneous minerals to a variable extent throughout the deposit, and thus allow for investigating the effects of post-cumulus alteration on the distribution of a wide range of chalcophile elements in a magmatic sulfide deposit at both whole-rock and mineral scale. This study presents the whole-rock distribution of S, platinum-group elements, and Te, As, Bi, Sb, and Se in both mineralization styles and the concentration of trace elements in base-metal sulfides from the Sulfide zone. The Sulfide zone has Pt/Pd ratios around 0.5 and high concentrations of Te, As, Bi, Sb, and Se, whereas the low-S-high-platinum-group element zone has Pt/Pd ratios greater than 1 and much lower Se, Te, and Bi concentrations, but comparable As and Sb contents. This is reflected in the platinum-group element assemblage, comprising bismuthotellurides in the Sulfide zone and mostly arsenides and antimonides in the low-S, high platinum-group elements zone. Moreover, the base-metal sulfides from the Sulfide zone have anomalously high As contents (50–500 ppm), which suggest that the sulfide liquid segregated from a very As-rich silicate magma, possibly illustrated by an average komatiitic basalt that assimilated a mixture of upper continental crust and black shales. We interpret the low-S-high platinum-group elements zone as a product of S loss from magmatic sulfides during post-cumulus alteration of the Luanga Complex. Selenium, Te, Bi, and Pd were also lost together with S, whereas As and Sb were expelled from base-metal sulfide structures and combined with platinum-group elements to form platinum-group minerals, suggesting they may play a role fixating platinum-group elements during alteration. The remobilization of chalcophile elements from magmatic sulfide deposits located in the Carajás Mineral Province may represent a potential source for hydrothermal deposits found in the region.

Keywords: Platinum-group elements, TABS+, magmatic sulfide deposits, post-cumulus alteration, low-S-high platinum-group elements.

[§] *Corresponding author e-mail address*: etmansur@gmail.com

Introduction

The behavior of chalcophile elements during the formation of magmatic Ni-Cu and platinum-group elements (PGE) deposits has been extensively studied (Holwell & McDonald 2010, Naldrett 2010, Barnes & Ripley 2016, Barnes *et al.* 2017). Several studies have also shown that different processes may affect the distribution of trace elements in base-metal sulfides (BMS), such as crustal assimilation (Dare *et al.* 2010a, Godel *et al.* 2012, Piña *et al.* 2015, Samalens *et al.* 2017a), fractional crystallization (Dare *et al.* 2010b, 2011, 2014, Mansur *et al.* 2020a), exsolution and crystallization of platinum-group minerals (PGM; Godel *et al.* 2007, Godel & Barnes 2008, Holwell & McDonald 2007, Barnes *et al.* 2008, Piña *et al.* 2012, Wirth *et al.* 2013, Osbahr *et al.* 2014, Junge *et al.* 2015, Mansur & Barnes 2020a), among others. These studies provided solid understanding on the composition of magmatic BMS, and thus allowed their use as indicator minerals for exploration in areas under cover (*e.g.*, McClenaghan *et al.* 2011, 2020, McClenaghan & Paulen 2018, Duran *et al.* 2019). However, fewer studies have concentrated on the effects of post-cumulate alteration on the distribution of chalcophile elements in magmatic deposits (Tao *et al.* 2007, Wang *et al.* 2008, Dare *et al.* 2011, Djon & Barnes 2012, Duran *et al.* 2015, Piña *et al.* 2016, Holwell *et al.* 2017, Junge *et al.* 2019), especially its effect on BMS compositions. Thus, our understanding of this subject can still be refined.

After BMS crystallization, a number of processes may change its composition, including: (1) Late magmatic fluids that may partially or completely dissolve the BMS, changing the initial BMS assemblage from pyrrhotite-pentlandite-chalcopyrite (Po-Pn-Ccp) to Pn-Ccp-pyrite (Py), then millerite-Ccp-Py (Djon & Barnes 2012, Holwell *et al.* 2017), possibly continuing until no or very little BMS is left. In the process, PGE that were originally accommodated in the BMS may combine with Te, As, Bi, Sb, or Sn and form various PGM (Wood 2002). (2) Degassing of sulfides close to surface may strip the sulfides of S, leaving only metals behind (Sluzhenikin *et al.* 2020). (3) Weathering may dissolve S and possibly Pd (Junge *et al.* 2015, 2019, Oppermann *et al.* 2017). (4) Metamorphism may introduce fluids that strip the BMS of S, leaving only PGM (Mota-e-Silva *et al.* 2015, Holwell *et al.* 2017). (5) Bismuthotelluride and antimonide PGM melt above 600°C and could be mobilized during high-grade metamorphism (Molnár *et al.* 2001, Helmy *et al.* 2007, Tomkins *et al.* 2007, Péntek *et al.* 2008, Dare *et al.* 2014, Tuba *et al.* 2014).

Understanding how different chalcophile elements behave during alteration of magmatic sulfide deposits, at both whole-rock and mineral scale, may also be important for assessing the formation of atypical PGE deposits. For example, although most PGE-dominated deposits are associated with disseminated sulfides and/or chromite-rich rocks (Naldrett 2004, Maier 2005, Barnes & Ripley 2016, and references therein), several contributions have highlighted the occurrence of PGE-rich rocks with very little or none of these minerals (Maier *et al.* 2003, Andersen 2006, Tao *et al.* 2007, Wang *et al.* 2008, Kaukonen 2008, Tuba *et al.* 2014, Maier *et al.* 2015, Barnes *et al.* 2016, Brzozowski *et al.* 2020, Mansur *et al.* 2020b, Sluzhenikin *et al.* 2020). These occurrences are normally referred to as low-sulfide PGE deposits and have been suggested to form by either the direct crystallization of PGM from the silicate magma (*e.g.*, Maier *et al.* 2015, Barnes *et al.* 2016), or by S loss from magmatic sulfides during alteration or degassing (Kaukonen 2008, Mansur *et al.* 2020b, Sluzhenikin *et al.* 2020). It is noteworthy that if these occurrences formed by S loss, other chalcophile elements may also have been lost, and may be remobilized by fluids (Patten *et al.* 2016, 2017, Holwell *et al.* 2017, 2019, Scholten *et al.* 2018).

The Luanga intrusion of the Carajás area, Brazil (Fig. 1), hosts two different styles of PGE mineralization, comprising a classic magmatic Ni-Cu-PGE deposit consisting of disseminated sulfides, the Sulfide zone, and several low-S-high-PGE zones which contain no sulfides but do contain a variety of PGM, as documented by Ferreira Filho *et al.* (2007) and Mansur *et al.* (2020b), who provide detailed field work descriptions, whole-rock geochemistry, and mineral chemistry of the main cumulus phases. The current work expands this data set with whole-rock S, PGE, and the chalcophile elements Te, As, Bi, Sb, and Se (from here on referred to as TABS+ to include Se, following in original definition proposed by Barnes & Ripley 2016), and the concentrations of trace elements in the BMS from the Sulfide zone. This allows us to compare and contrast the two styles of mineralization in the same intrusion and to investigate the effects of post-cumulus alteration on the distribution of chalcophile elements at both whole-rock and mineral scales.

This work will show that the low-S-high-PGE zone formed by the post-cumulus loss of S from the magmatic sulfides. Together with S, at least part of Se, Te, Bi, and Pd were also remobilized by post-cumulus fluids. In contrast, As and Sb combined with PGE to form the PGM and likely acted as fixing agents for these elements during alteration as proposed theoretically by Wood (2002).

Regional Setting

The Carajás Mineral Province (CMP) is located at the eastern margin of the Amazon Craton (Fig. 1a).

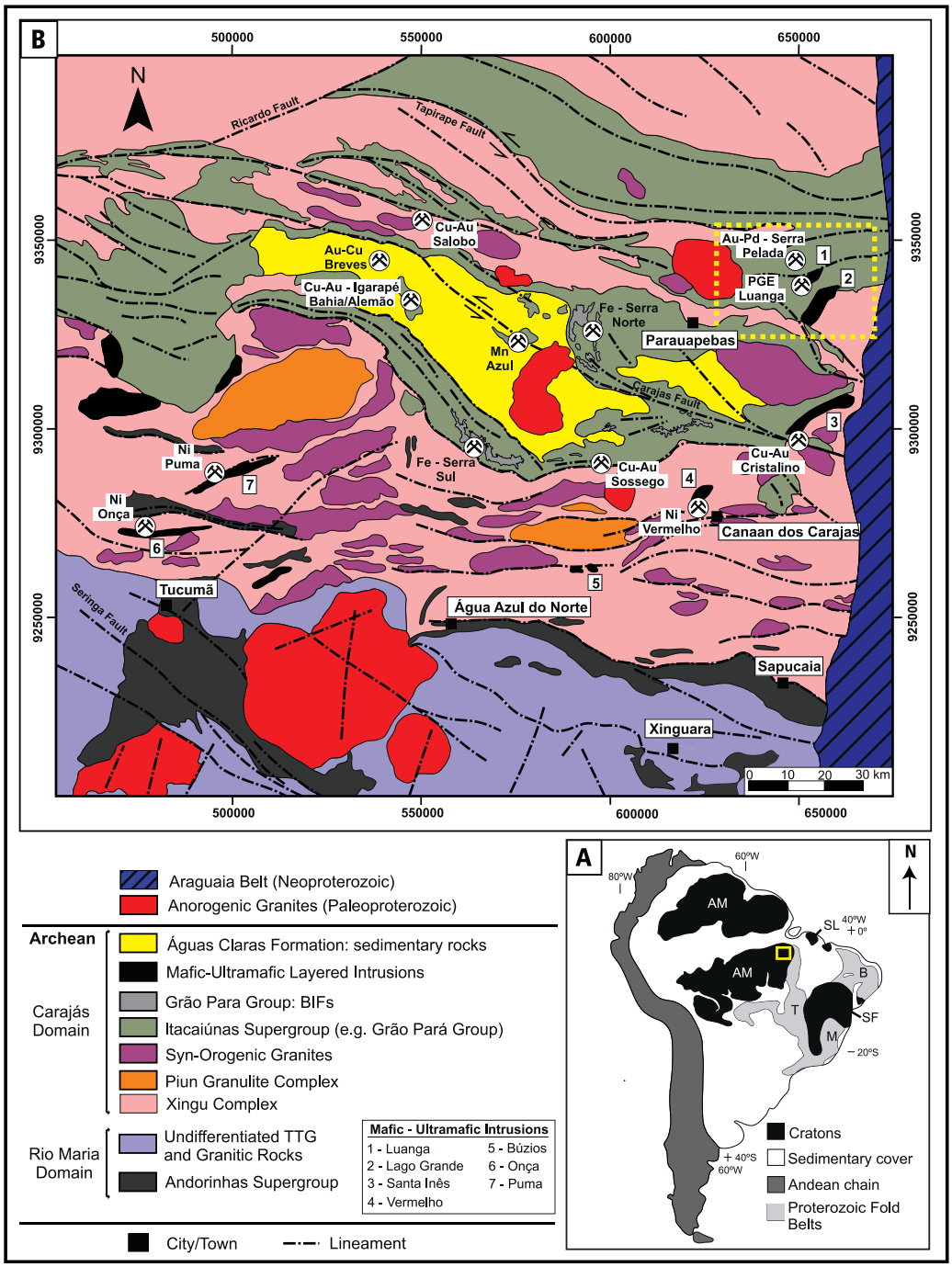

FIG. 1. Geological setting of the Carajás Mineral Province. (a) Location of the Carajás Mineral Province. AM – Amazon Craton; B – Borborema Province; M – Mantiqueira Province; SF – São Francisco Craton; T – Tocantins Province. (b) Geological map of the Carajás Mineral Province (modified from Vasquez *et al*. 2008). The dashed rectangle indicates the location of the Serra Leste magmatic suite.

The province has become widely known due to several important mineral deposits, including iron oxide copper-gold (IOCG), Ni deposits, and the largest iron resources in the world (*e.g.*, Dardenne & Schobbenhaus 2001, Grainger *et al*. 2008, Xavier *et al*. 2010, Moreto *et al*. 2015). The Carajás province is subdivided into two Archean tectonic domains, the Rio Maria Domain to the south and the Carajás Domain to the north (Fig. 1b; Vasquez *et al*. 2008).

In the Carajás Domain, several 2.75 Ga mafic–ultramafic layered complexes intrude the Xingu Complex and Archean volcano-sedimentary sequences, which represent the basement rocks (Fig. 1b; Docegeo 1988, Ferreira Filho *et al*. 2007). Although Ni laterite deposits are found to the western portion of the province (*e.g.*, Puma and Vermelho complexes; Ferreira Filho *et al*. 2007, Rosa 2014, Siepierski & Ferreira Filho 2020; Fig, 1b), the PGE-mineralized layered intrusions are limited to the eastern portion of the province. These PGE-mineralized intrusions are grouped into the Serra Leste magmatic suite, and the Luanga deposit, which hosts the largest PGE resources in South America (142 Mt at 1.24 ppm Pt + Pd + Au and 0.11% Ni; Mansur *et al*. 2020b). Detailed descriptions of the Serra Leste magmatic suite are provided by Teixeira *et al*. (2015) and Mansur & Ferreira Filho (2016, 2017). A brief overview of the Luanga deposit is provided below.

The Luanga Complex and Previous Studies

The Luanga Complex is a 6 km long and up to 3.5 km wide layered intrusion (Fig. 2a). Considering the original stratigraphy, from base to top, the intrusion consists of ultramafic cumulates (Ultramafic zone), an intercalation of ultramafic and mafic cumulates (Transition zone) and mafic cumulates (Mafic zone; Fig. 2b; Mansur & Ferreira Filho 2016). The Ultramafic zone overlies the Transition zone, which overlies the Mafic zone, indicating that the layered sequence is tectonically overturned (Fig. 2b). Metamorphic assemblages commonly replace primary igneous minerals and indicate temperatures of upper greenschist to lower amphibolite facies. This metamorphic alteration is characterized by an extensive hydration that largely preserves primary textures, bulk rock compositions, and the compositional domains of igneous minerals. These assemblages are serpentine + talc + magnetite ± cummingtonite in the peridotites; talc + serpentine + magnetite ± cummingtonite in the orthopyroxenites; and hornblende + chlorite + epidote in the mafic rocks (Ferreira Filho *et al*. 2007, Mansur & Ferreira Filho 2016).

The bulk of the PGE resources of the Luanga Complex comprise two distinct styles of mineralization located mainly in the Transition zone (Fig. 2b; Mansur *et al*. 2020b). The first, termed the Sulfide zone, hosts the bulk of PGE resources of the Luanga Complex (*i.e.*, 142 Mt at 1.24 ppm Pt + Pd + Au and 0.11% Ni; Mansur *et al*. 2020b) and consists of a 10 to 50 m-thick interval located at the contact between the Ultramafic and Transition zones with 1 to 5% disseminated base metal sulfides (Pn>Po>>>Ccp; Fig. 3a). The Sulfide zone comprises not only pristine magmatic sulfides, but also includes mineral assemblages with different degrees of alteration, for example, the occurrence of silicate lamellae intergrowth with sulfide minerals, and commonly observed magnetite rims (Fig. 3b and 3c). These alteration assemblages are constrained to local zones and do not form specific horizons within the intrusion. The sulfide mineralogy itself does not show significant variation, but the local occurrence of pyrite in more altered assemblages is observed (Mansur *et al*. 2020b). The second zone, termed the low-S-high-PGE zone, occurs in a series of discontinuous lenses 1 to 5 m-thick within the Transition zone, consisting of sulfide- and chromite-free harzburgite and orthopyroxenite that do not show any distinctive textures relative to barren rocks (Fig. 3d). Therefore, these PGE-enriched intervals were not identified during core logging or petrographic studies, but only by their anomalous Pt-Pd contents on assay (Mansur *et al*. 2020b).

In terms of PGM, the Sulfide zone contains predominantly Pt-Pd bismuthotellurides, stanides, and arsenides, mainly enclosed within or at the contact with sulfide minerals (Figs. 3e, 4a, and 4b). In contrast, the PGM observed in the low-S-high-PGE zone are mainly Pt-arsenides and antimonides, mostly enclosed within secondary silicates (Figs. 3f, 4c, and 4d). Mansur *et al*. (2020b) interpreted these features to be the result of segregation of an immiscible sulfide liquid that formed both zones and that the low-S-high-PGE zone had subsequently lost S during post-cumulus alteration, and likely represents the final product of an extensive alteration of the Sulfide zone. For a more comprehensive characterization of PGM assemblages found in both PGE zones, the readers are referred to Mansur *et al*. (2020b)

Methodology

Our samples were selected from the collection described by Mansur *et al*. (2020b), which comprises core from drill holes from the central and northern portion of the Luanga Complex (Fig. 2a and 2b). This previous study provided the geological background and detailed sample description necessary for our current investigation. Twenty-five samples were chosen to reflect the representative features observed in

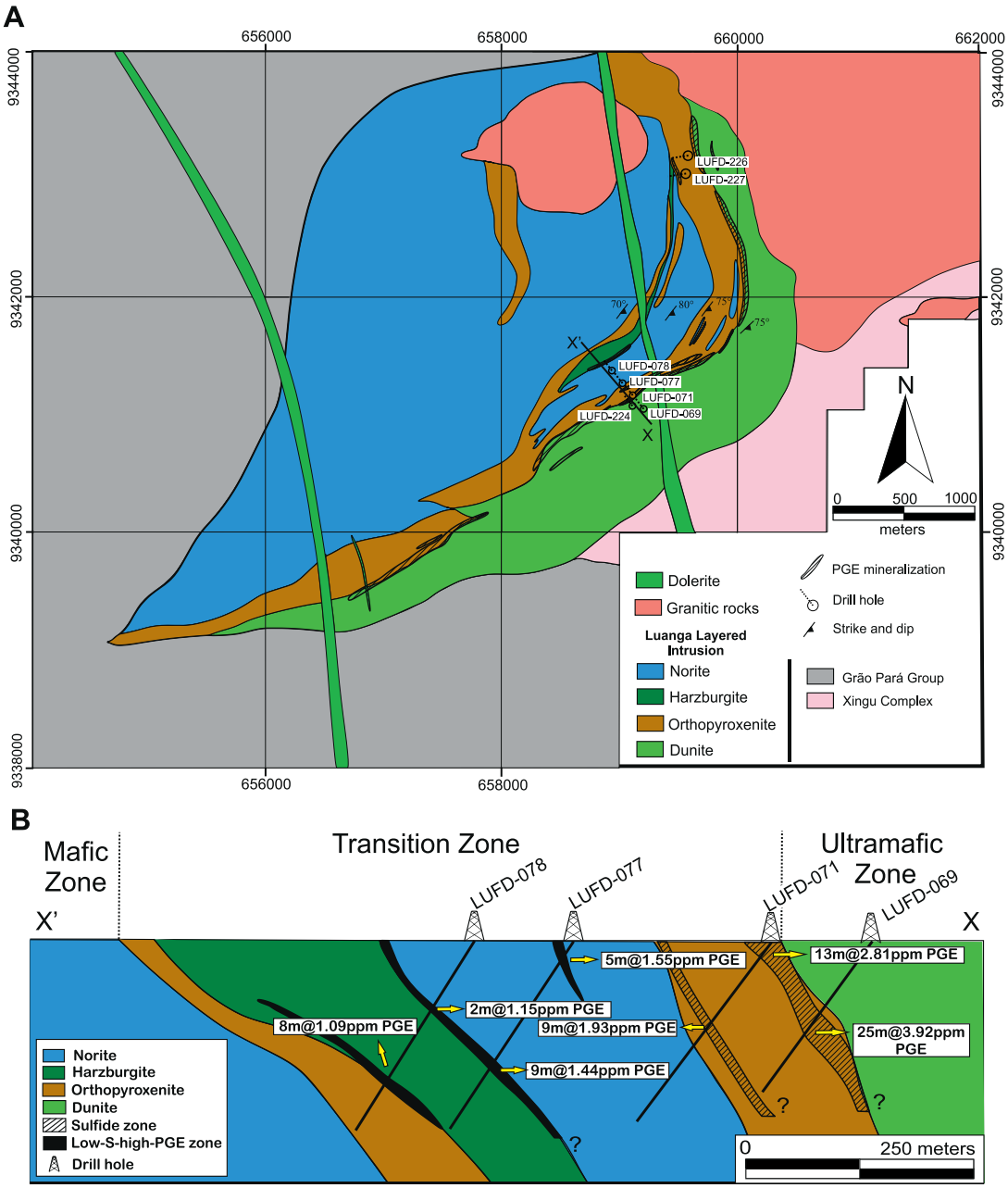

FIG. 2. Local geology of the Luanga Complex. (a) Geological map of the Luanga Complex (partially modified from unpublished report of VALE). Note the location of drill holes referred to in this study. (b) Geological section at the central portion of the Luanga Complex. Abbreviations: PGE = ΣPt,Pd,Rh,Ru,Ir,Os. Figure partially modified from Mansur *et al.* (2020b).

the Luanga deposit, including rocks from the Sulfide zone (13 samples), the low-S-high-PGE zone (eight samples), and PGE-barren horizons (four samples). These samples enabled us to investigate the variations in whole-rock PGE and TABS+ between the different zones and the concentrations of trace elements in BMS from the Sulfide zone.

Platinum-group elements (Os, Ir, Ru, Rh, Pd, and Pt) and S were analyzed at LabMaTer, Université du Québec à Chicoutimi (UQAC). The PGE were pre-

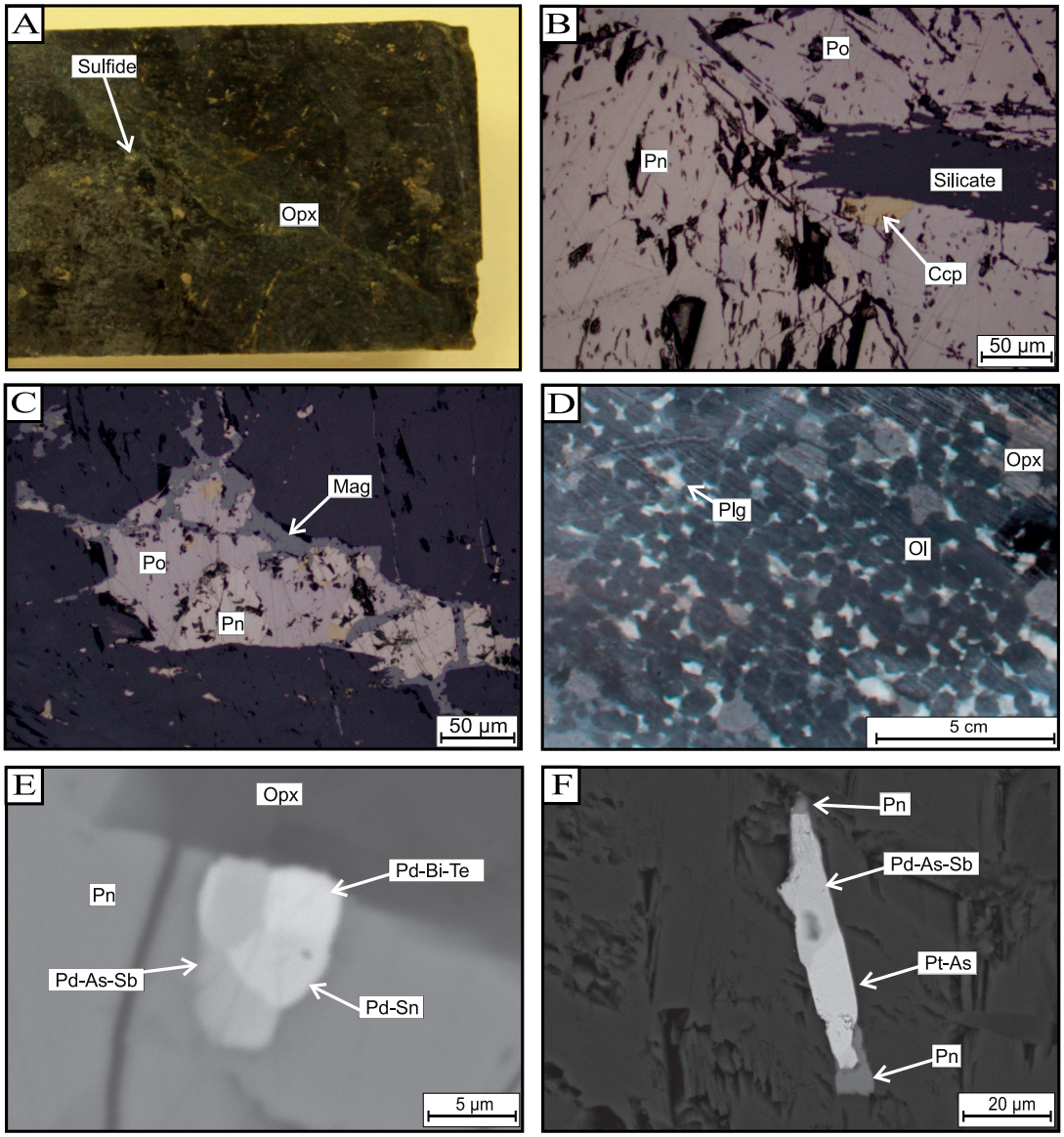

FIG. 3. General aspects of the Luanga deposit. (a) Core sample of orthopyroxenite from the Sulfide zone with cumulus orthopyroxene disseminated base metal sulfides. (b) Photomicrograph of a typical sulfide assemblage of the Sulfide zone with pentlandite, pyrrhotite, and chalcopyrite. Note the sulfide intergrowth with silicate lamellae. (c) Photomicrograph of base metal sulfides assemblage of the Sulfide zone with secondary magnetite around boundaries and along fractures. (d) Core sample of harzburgite from the low-S-high-PGE zone. The harzburgite consists of cumulus olivine and intercumulus orthopyroxene and plagioclase. (e) Backscattered image of round-shaped composite PGM grain comprising Pd-Bi-Te, Pd-As-Sb, and Pd-Sn at the contact between pentlandite and orthopyroxene. (f) Backscattered image of elongated PGM grain comprising Pt-As and Pd-As-Sb with minor Pn grains at grain edges. The PGM grains are enclosed within the cleavage of secondary chlorite grains. Ccp: chalcopyrite; Mag: Magnetite; Ol: olivine; Opx: orthopyroxene; Pn: Pentlandite; Plg: Plagioclase; Po: Pyrrhotite.

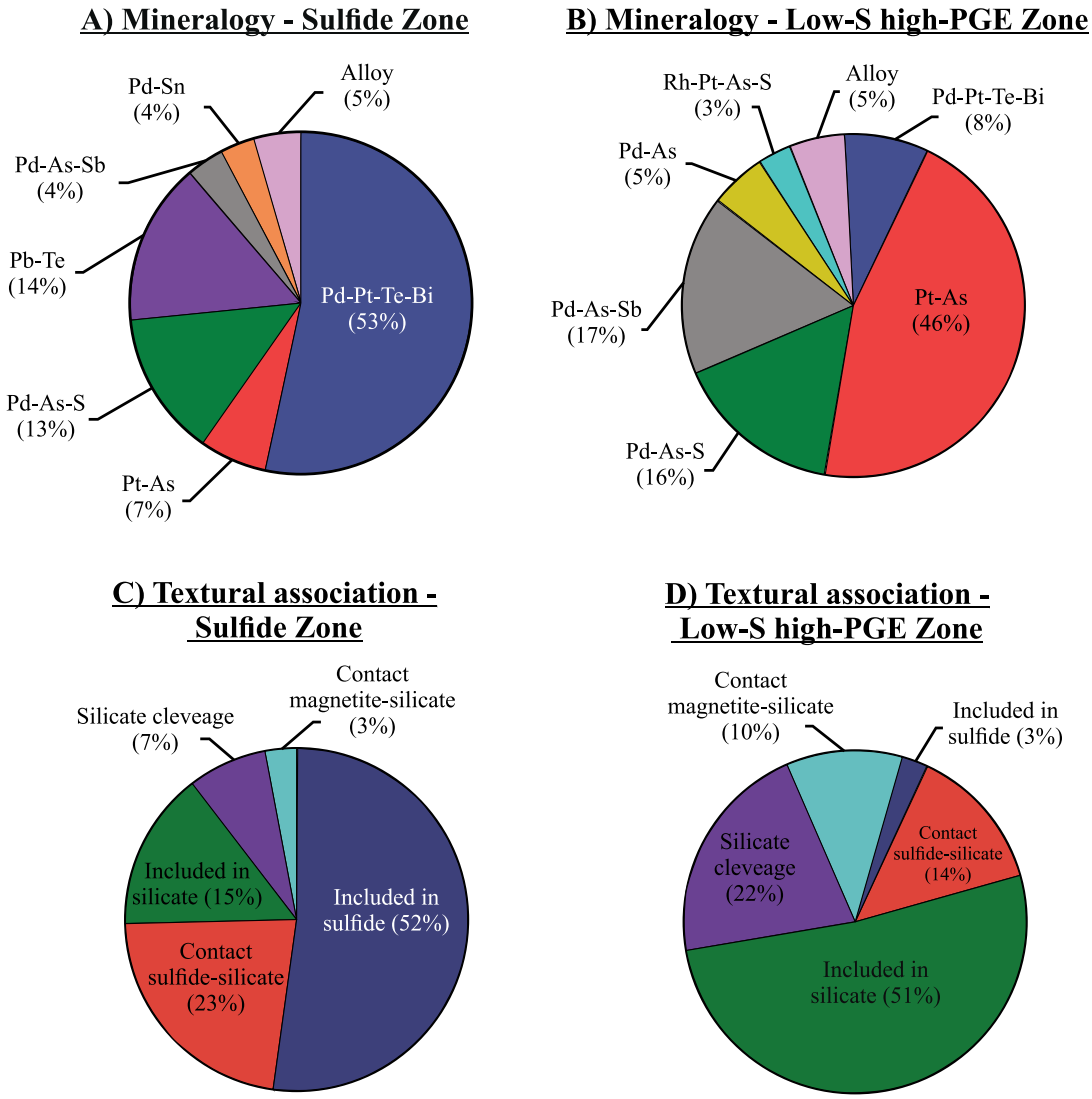

FIG. 4. Pie charts summarizing the proportion of each PGM and precious-metals mineral (PMM) within the (a) Sulfide zone, and (b) low-S-high-PGE zone; and textural association of these minerals within the (c) Sulfide zone and (d) low-S-high-PGE zone of the Luanga Complex. Figure partially modified from Mansur *et al.* (2020b).

concentrated by Ni-sulfide fire assay followed by co-precipitation with Te and were analyzed by solution inductively coupled plasma-mass spectrometry (ICP-MS) using the method described by Savard *et al.* (2010). Sulfur was determined *via* combustion and infrared analysis using a HORIBA EMIA-220V analyzer and the method described by Bédard *et al.* (2008). International reference materials (OKUM and GeoPT-18/KPT-1, from IAGEO; LK-NIP-1 and LDI-1, from Geo Labs - OGS) were analyzed with the samples to monitor data quality. The results obtained for the reference materials are consistent with the working values (electronic supplementary material (ESM)[1], Table 1).

Tellurium, As, Bi, Sb, and Se analyses were obtained using Hydride Generation-Atomic Fluores-

[1] Supplementary Data are available from the Depository of Unpublished Data on the MAC website (http://mineralogicalassociation.ca/), document "Luanga Deposit, Brazil, CM59, 21-00018".

cence Spectrometry (HG-AFS) following the technique described by Mansur *et al*. (2020c), also at LabMaTer, UQAC. International reference materials (CH-4 and TDB-1 from Natural Resources Canada; OKUM from IAGEO) and a blank were measured at the same time as the samples, and the results agree with the working values (ESM, Table 2). The 3σ detection limits are 0.006, 0.003, 0.007, 0.009, and 0.003 ppm for Te, As, Bi, Sb, and Se, respectively.

The concentration and distribution of minor and trace elements in the sulfide minerals were determined by laser ablation-inductively coupled plasma-mass spectrometry (LA-ICP-MS) at LabMaTer (UQAC) using an Excimer 193 nm RESOlution M-50 laser ablation system (Australian Scientific Instrument) equipped with a double-volume cell S-155 (Laurin Technic) and coupled with an Agilent 7900 mass spectrometer. The LA-ICP-MS tuning parameters were a laser frequency of 10 Hz, a power of 3 to 5 mJ/pulse, a dwell time of 7.5 ms, a rastering speed of 5 to 10 μm/s, and a fluence of 3 J/cm^2. Line scans across the surface of grains were made with beam sizes of both 33 and 44 μm, depending on the grain size. The gas blank was measured for 20 to 30 s before switching on the laser for around 60 s. The ablated material was carried into the ICP-MS by an Ar–He gas mix at a rate of 0.8 to 1 L/min for Ar and 350 mL/min for He (an additional 2 mL/min of nitrogen was also added to the mixture). Data reduction was carried out using the Iolite package for Igor Pro software (Paton *et al*. 2011).

^{57}Fe values obtained from microprobe results for the different sulfide minerals by Mansur & Ferreira Filho (2016) were used for internal standardization. Three certified reference materials were used for external calibration of the BMS: Laflamme Po727, a synthetic FeS doped with ~40 ppm PGE and Au supplied by Memorial University of Newfoundland, was used to calibrate for PGE, Au, and S; MASS-1, which is a ZnCuFeS pressed powder pellet doped with 50 to 70 ppm of most chalcophile elements, supplied by the United States Geological Survey (USGS), was used to calibrate for Co, Cu, Zn, As, Se, Mo, Ag, Cd, Sn, Sb, Te, Tl, Pb, and Bi; and GSE-1g, which is a natural basaltic glass fused and doped with most elements at 300 to 500 ppm and supplied by the USGS, was used to calibrate for Ni, In, and Re using preferred values from the GeoReM database (Jochum *et al*. 2005). MASS-1, GSE-1g, JB-MSS5 (an FeS sulfide containing 50 to 70 ppm of most chalcophile elements, supplied by James Brenan) and UQAC-FeS1 (a synthetic sulfide developed at UQAC) were used to monitor the results. The results obtained for these standards were generally in good agreement with the accepted values (ESM, Table 3).

Polyatomic interference of ^{63}Cu^{40}Ar on ^{103}Rh was corrected using ^{103}Rh measured in MASS-1, which contains 13.4% ^{63}Cu but no ^{103}Rh. One percent Cu produced ~0.1 ppm interference. Thus, the ^{103}Rh values in Ccp are not reported as the interference is too large to be corrected. Direct interferences of ^{108}Cd on ^{108}Pd and ^{115}Sn on ^{115}In were corrected by monitoring ^{111}Cd and ^{118}Sn, respectively. Interference of ^{68}Zn^{40}Ar on ^{108}Pd is negligible as Zn is present at <1000 ppm. Polyatomic interference of ^{61}Ni^{40}Ar on ^{101}Ru was corrected using ^{101}Ru measured in a NiS blank, which does not contain Ru. One percent Ni produced ~ 0.007 ppm interference and was not a significant part of the Ru signal.

Maps of element distribution were made using a laser frequency of 15 Hz and a power of 5 mJ/pulse. The beam size (33 μm) and the stage movement speed (15 μm/s) were adapted to optimize spatial resolution and analysis time for grain sizes. The maps were generated using the Iolite software package on the basis of the time-resolved composition of each element. The maps indicate the relative concentration of the elements and are semi-quantitative.

Results

Whole-rock PGE and TABS+ distribution

The distribution of PGE in whole rocks from the Luanga deposit has been previously considered by Mansur *et al*. (2020b) using the results from exploration boreholes. Here we provide a new set of whole-rock PGE and S results using methods with better precision, and lower detection limits, and also provide the first results for TABS+ in the deposit. The whole-rock results for PGE, S, and TABS+ obtained in this study, plus the previously published Ni, Cu, Co, and Cr concentrations, can be found in the electronic supplementary materials (ESM, Table 4).

Most of the samples display similar mantle-normalized Ni, PGE, Au, and Cu patterns, with IPGE (Ir, Os, and Ru) depletion relative to PPGE (Pt, Pd, and Rh) and Au, and negative Cu anomalies (Fig 5a). The patterns for the Sulfide zone range from 1 to 20 times mantle values for Ni and IPGE, to around 10 to 1000 times mantle for Au and PPGE, with Cu values mostly varying from 1 to 10 times mantle (Fig. 5b). The patterns for the low-S-high-PGE zone are lower by an order of magnitude (Fig. 5c), followed by the patterns for the barren rocks (Fig. 5d), which are the lowest. One of the barren samples is a serpentinite and has a relatively flat pattern close to mantle values.

The distribution of TABS+ was also assessed using a mantle-normalized spidergram with the elements organized, from left to right, in order of partition coefficients between sulfide and silicate liquid (Barnes

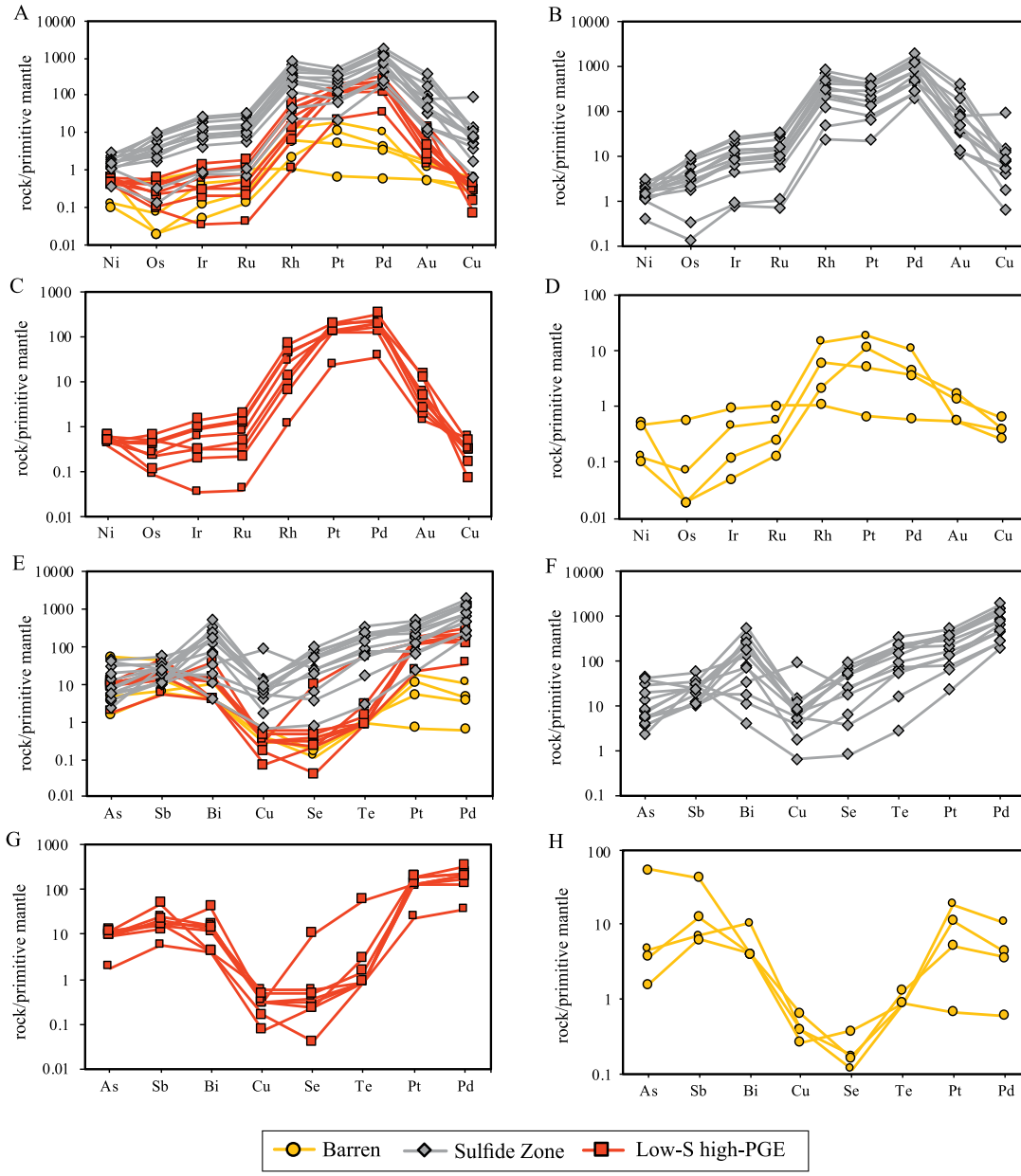

FIG. 5. Primitive mantle-normalized Ni–PGE–Au-Cu (a, b, c, and d) and TABS-Pt-Pd (e, f, g, and h) patterns of samples from different zones of the Luanga Complex (a and b), and shown separately for the Sulfide zone (b and f), low-S-high-PGE zone (c and g), and barren rocks (d and h). Primitive mantle values from Lyubetskaya & Korenaga (2007). Whole-rock results are given in the electronic materials (ESM, Table 4).

2016). Copper, Pt, and Pd were also included in the diagram to consider the possible effects of sulfide segregation and or alteration (Barnes & Mansur, *in press*).

Samples from the Sulfide zone have a different pattern than those from the low-S-high-PGE zone and barren rocks (Fig. 5g and 5h). The mantle-normalized patterns for the Sulfide zone display a positive slope

from 1 to 100 times mantle at As to 100 to 1000 times mantle at Pd, with slightly positive Bi and negative Cu anomalies (Fig. 5f). The low-S-high-PGE zone and barren rocks patterns display As and Sb between 1 and 50 times mantle, strong Cu, Se, and Te negative anomalies, and Pt and Pd from 10 to 100 times mantle for the low-S-high-PGE zone (Fig. 5g), and 1 to 10 for the barren rocks (Fig. 5h).

There are positive correlations between S and Se for most of the Sulfide zone and barren samples (Fig. 6a), whereas most rocks from the low-S-high-PGE zone have S values below detection limits (Fig. 6a) and do not define a clear trend. The samples from both the low-S-high-PGE zone and most of the Sulfide zone plot above the solid line representing primitive mantle values (around 3050; Lyubetskaya & Korenaga 2007). In the case of the Sulfide zone the low S/Se ratios (average 2500) may be the result of S loss (Lesher & Burnham 2001, Hinchey & Hattori 2005, Queffurus & Barnes 2015), but because Se has a high partition coefficient into sulfide liquid (Liu & Brenan 2015) they could also be the result of the sulfide liquid forming at a high *R*-factor. In the case of the low-S-high-PGE zone the average ratio is <2000 and more probably represent the effects of S loss as argued by Mansur *et al*. (2020b). In contrast, barren samples have S/Se ratios slightly greater than mantle values. These higher ratios (6400) could be the result of the magma having previously segregated a sulfide liquid and depleted the magma in Se as observed in the Upper Zone of the Bushveld Complex (Barnes *et al*. 2009) or could be contamination of the magma with a sediment which would tend to enrich the magma in S over Se (Queffurus & Barnes 2015).

In order to avoid the artifacts of S loss and because the precision of the Se analyses is higher than that of the S analyses, Se is used in the following plots as a proxy for S. There is a broad positive correlation between Pt, Pd, and Se for most samples from the Sulfide zone, however, Pd and Pt are enriched in samples from the low-S-high-PGE zone relative to Se compared to the Sulfide zone (Fig. 6b and 6c). Rh and IPGE show a similar positive correlation in samples from the Sulfide zone (Fig. 6d to 6g). Tellurium is below the detection limit for most samples (0.007 ppm) from the low-S-high-PGE zone and barren rocks, whereas it shows a positive correlation with Se in samples from the Sulfide zone (Fig. 6h). For the Sulfide zone the Se/Te ratios are lower than mantle values (around 8 to 9; Lyubetskaya & Korenaga 2007), which is explained by the higher partition coefficient of Te into the sulfide liquid relative to Se (Patten *et al*. 2013, Liu & Brenan 2015). Bismuth also shows a broad positive correlation with Se, but a few samples from the Sulfide zone have relatively lower Bi contents (Fig. 6i). In contrast, As and Sb show no clear correlation with Se (Fig. 6j and 6k) but do correlate with each other (not shown), thus suggesting that sulfides are not the main minerals controlling their distributions.

The whole-rock correlations among different chalcophile elements in the Luanga deposit are shown in Figure 7. Platinum and Pd show good positive correlations within each zone, with Pt/Pd ratios lower in the Sulfide zone (0.5) than in the low-S-high-PGE zone (1 to 1.5) and barren rocks (>2). Palladium and Ir also show a good positive correlation within the Sulfide zone with a Pd/Ir ratio close to 100 (Fig. 7b), however the Pd/Ir ratios are variable and remarkably high, up to 1000 for the low-S, high-PGE zones (Fig. 7b). Similarly, within the Sulfide zone Pd and Pt correlate with IPGE (represented by Ru), with the low-S-high-PGE zone having lower Pt or Pd to IPGE ratios than the Sulfide zone (Fig. 7c). Rhodium shows a positive correlation with IPGE (Fig .7d), and the IPGE also show a good inter-element correlation (Fig. 7e).

The relation between TABS+ and PGE is more variable. Platinum and Pd have a positive correlation with both As and Sb in the low-S-high-PGE zone, and the ratios between these elements are close to the ratios for $PtAs_2$ and Pd(As,Sb), which have both been identified as PGM present in the Luanga deposit (Figs. 3e and f), indicating that these are the main phases controlling Pt and Pd distribution (Figs. 7i and j). In the Sulfide zone, Pt also shows a positive correlation with Te and Bi, and their ratios are similar to $Pt(Bi,Te)_2$ showing that it is the main phase controlling Pt distribution (Fig. 7i). However, although Pd shows no correlation with As and Sb in the Sulfide zone (Fig. 7j), it shows a broad positive correlation with both Te and Bi, supporting that Pd(Bi,Te) and $Pd(Bi,Te)_2$ are important phases affecting its distribution (Fig. 7k). This is also in agreement with the observed PGM assemblage, which is dominated by bismuthotellurides in the Sulfide zone, whereas it comprises mainly arsenides and antimonides in the low-S-high-PGE zone (Fig. 4).

Distribution of chalcophile elements among base metal sulfides

Median concentrations of trace elements in Po, Pn, and Ccp from each sample from the Sulfide zone, and the full LA-ICP-MS data set are reported in ESM, Tables 5–7. Typical time-signal diagrams show flat patterns for all of the elements, illustrating their homogeneous distribution within the BMS (*e.g.,* Fig. 8a to 8c). In some cases, the time-signal diagrams show peaks for some elements, indicating inclusions of PGM within BMS (*e.g.*, Fig. 8d). These inclusions

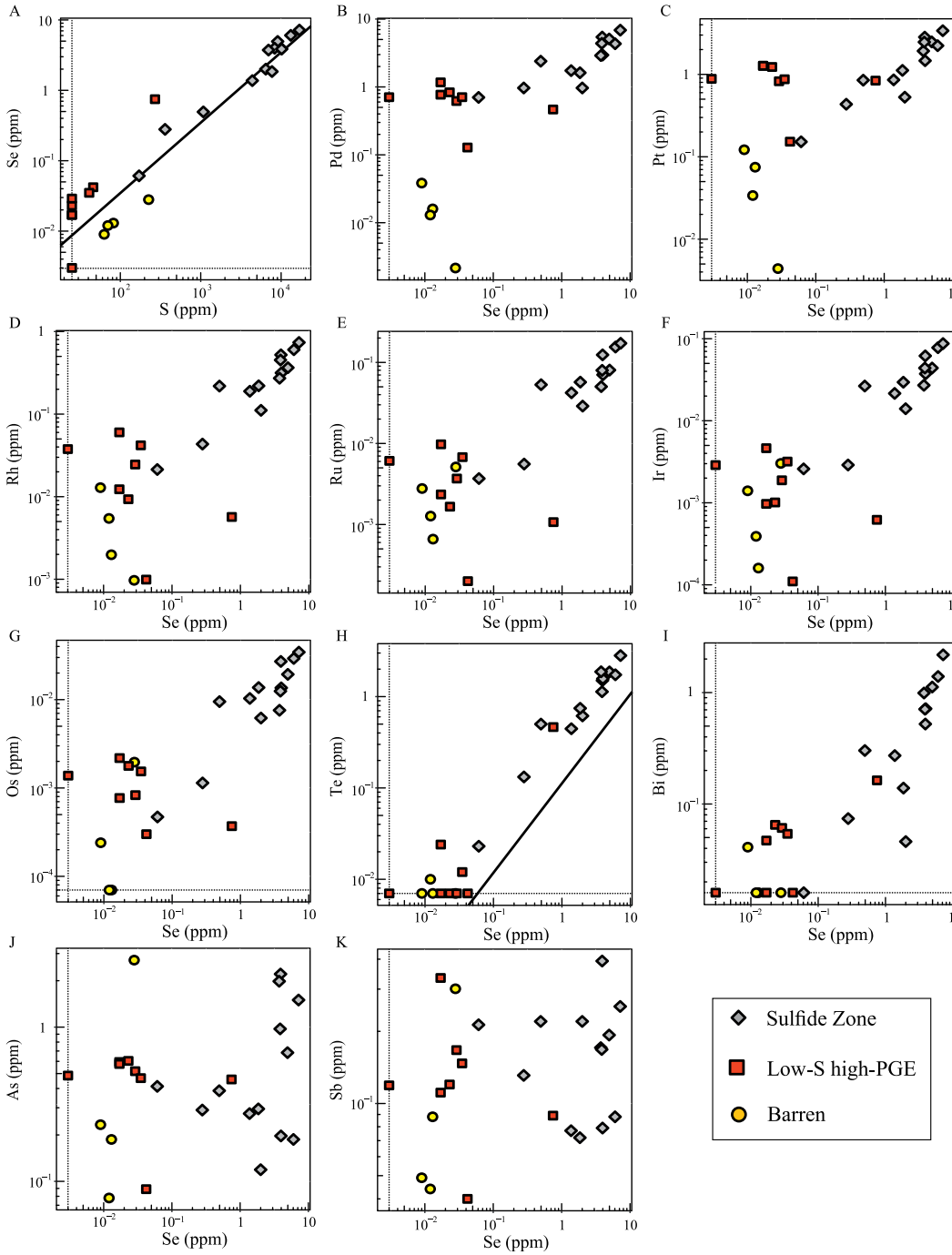

FIG. 6. Binary plots of (a) Se *versus* S and (b) Pd, (c) Pt, (d) Rh, (e) Ru, (f) Ir, (g) Os, (h) Te, (i) Bi, (j) As, and (k) Sb *versus* Se for samples from the Luanga Complex. The black line represents primitive mantle ratio (Lyubetskaya & Korenaga 2007) and dashed lines indicate the detection limits. Whole-rock results are given in the electronic materials (ESM, Table 4).

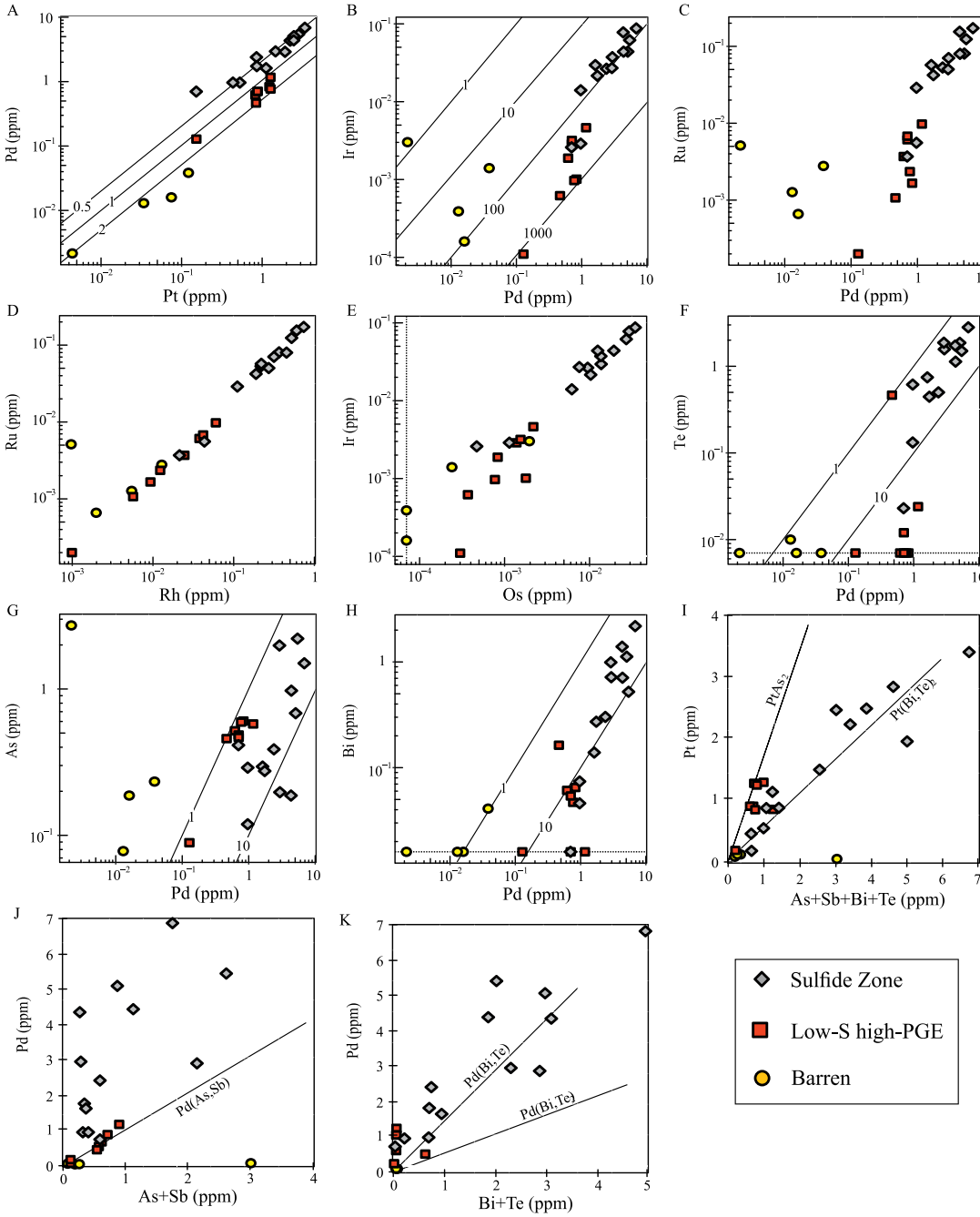

FIG. 7. Binary plots of (a) Pd *versus* Pt, (b) Ir *versus* Pd, (c) Ru *versus* Pd, (d) Ru *versus* Rh, (e) Ir *versus* Os, (f) Te *versus* Pd, (g) As *versus* Pd, (h) Bi *versus* Pd, (i) Pt *versus* As+Sb+Bi+Te, (j) Pd *versus* As + Sb, (k) Pd *versus* Bi + Te for samples from the Luanga Complex. The black line represents different ratios between elements and dashed lines indicate the detection limits. Whole-rock results are given in the electronic materials (ESM, Table 4).

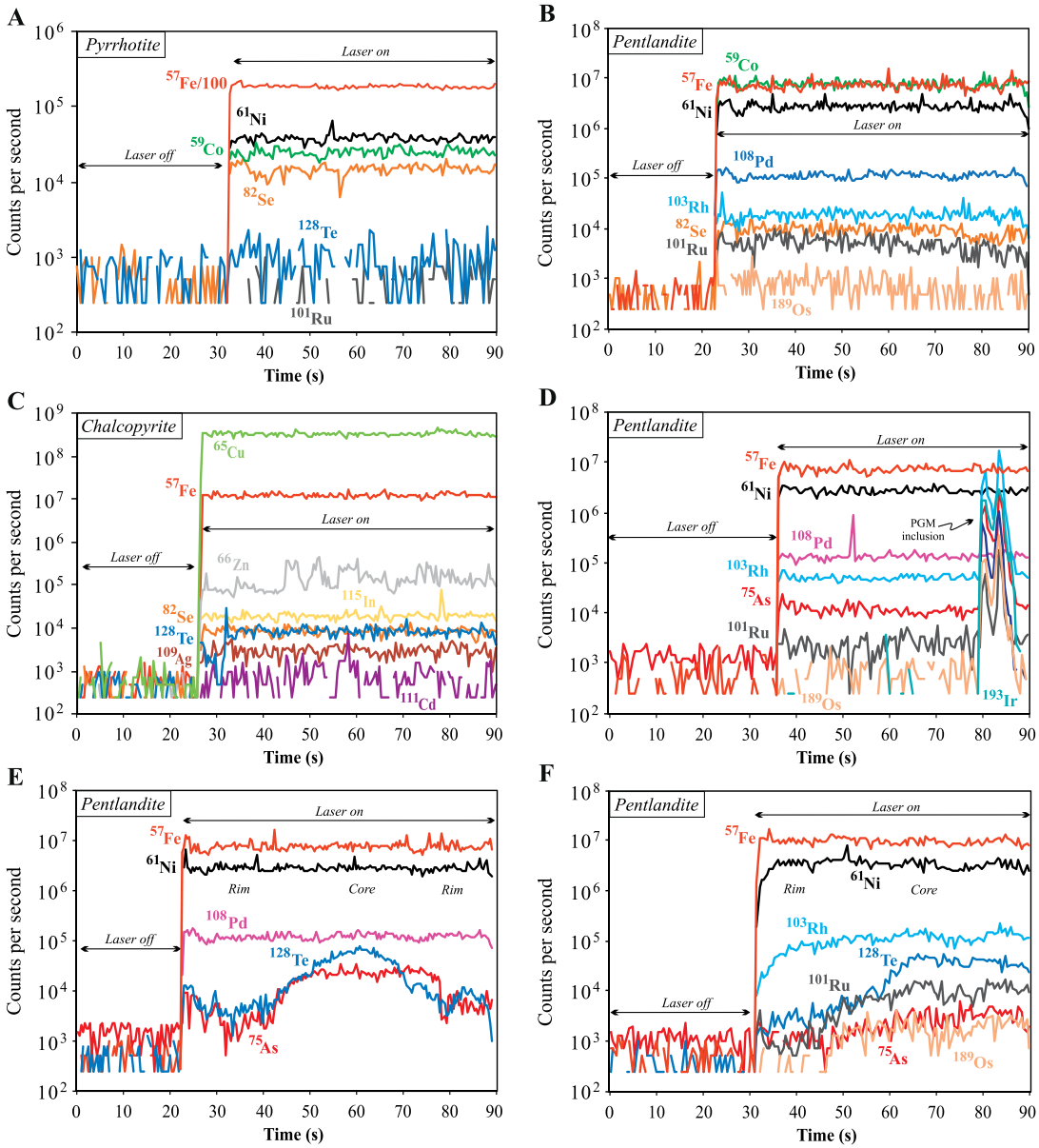

FIG. 8. Time (seconds) *versus* counts spectra for LA-ICP-MS analyses of BMS from the Sulfide zone of the Luanga deposit. (a) Pyrrhotite containing Fe, Ni, Co, Se, Te, and Ru in solid solution. (b) Pentlandite containing Co, Fe, Ni, Se, Ru, Rh, and Pd in solid solution. (c) Chalcopyrite containing Cu, Fe, Zn, Se, Ag, and Te in solid solution, with variations in Zn contents across the grain. (d) Pentlandite hosting an inclusion of Rh-Ru-Ir-Os-As, intersected by the laser at 80–87 s. (e) Pentlandite displaying compositional zonation with Te and As concentrations decreasing from core toward the borders of the grains. (f) Pentlandite displaying compositional zonation with Rh, Ru, Os, Te, and As concentrations decreasing from core toward the borders of the grains.

were not included in the integration that calculated the BMS compositions. The time-signal diagrams also make it possible to assess the zonation profiles displayed by some elements. For example, in many cases As and Te show zonation profiles in Pn grains with concentrations progressively decreasing from grain core toward boundaries (Fig. 8e). In a few cases Rh and IPGE zonation profiles are also present within

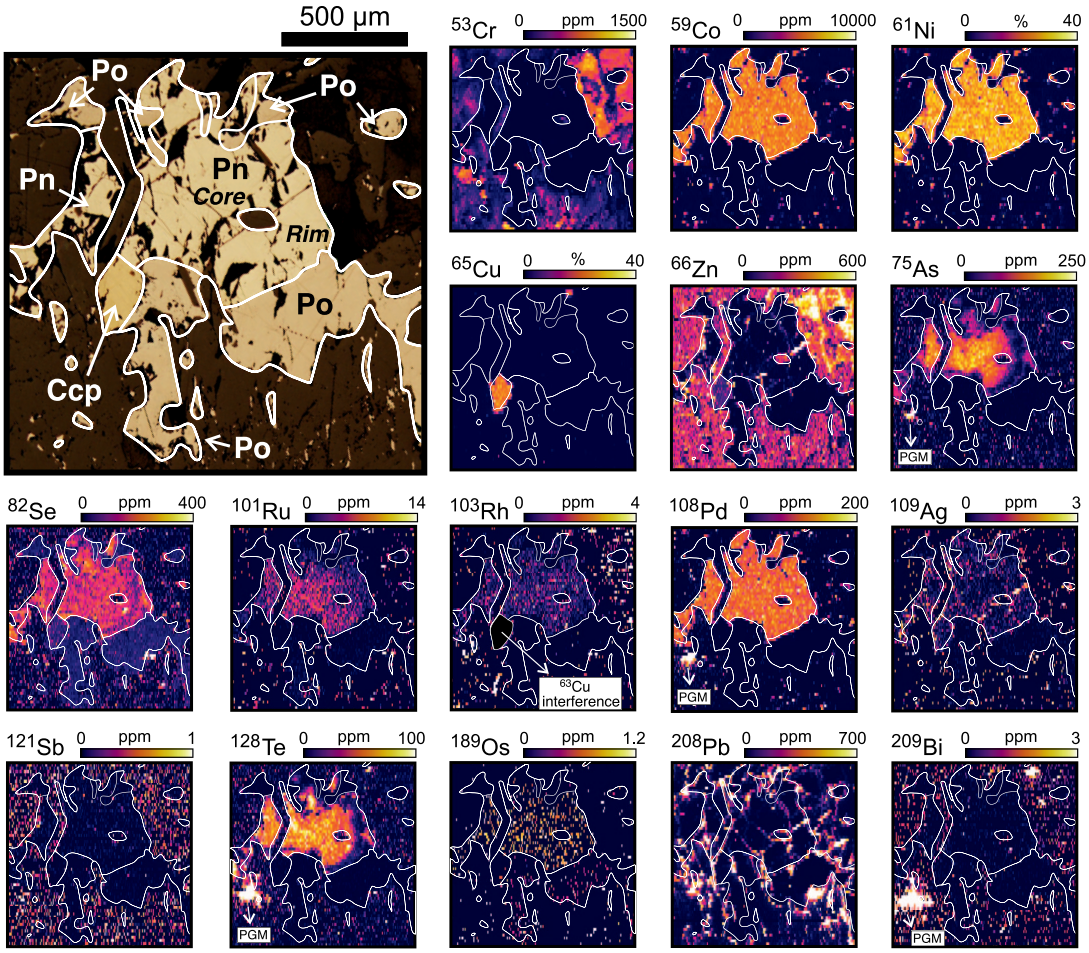

FIG. 9. LA–ICP-MS elemental maps showing the distribution of chalcophile elements among pyrrhotite (Po), pentlandite (Pn), and chalcopyrite (Ccp) in disseminated sulfide from the Sulfide zone of the Luanga deposit. The host silicate mineral is an amphibole. Note the PGM inclusions intersected by the laser leading to very high Pd, As, Te, and Bi concentrations. White lines show the grain outlines. The relative concentrations of the elements are semi-quantitative.

Pn grains (Fig. 8f). Compositional LA-ICP-MS maps of typical BMS assemblages from the Sulfide zone, comprising Po, Pn, and Ccp, are shown in Figure 9.

The LA-ICP-MS compositional maps show that Co, Ni, As, Ru, Rh, Pd, and Te are preferentially concentrated in Pn, whereas Cu and Zn are concentrated in Ccp (Fig. 9). Silver is distributed between Pn and Ccp, and Os is distributed between Po and Pn, but shows a preference for Pn. Selenium is present in all the BMS, but higher concentrations are found in Pn. Chromium, Zn, and Sb are also present in the surrounding silicates, which are mainly orthopyroxene and secondary chlorite. Lead and Bi occur mainly at grain boundaries and fractures, suggesting their local remobilization. The distribution of the trace elements in Pn is not homogeneous and higher concentrations of As, Se, Ru, and Te are observed in the grain core relative to the edges. Zonation patterns in Pn were previously observed elsewhere and argued to result from the formation of Pn by peritectic reaction at higher temperatures (Kitakaze *et al*. 2016, Mansur *et al*. 2019, Barnes *et al*. 2020). Alternatively, this texture could result from Pn alteration at grain boundaries and thus preferential loss of some elements. It is noteworthy that the depletion in As, Se, Ru, and Te in Pn is more evident where the grain is in contact with surrounding silicates (Fig. 9), supporting their loss during post-cumulus alteration. The effects of sulfide alteration on the distribution of chalcophile elements are discussed below.

The concentrations of trace elements in Po, Pn, and Ccp are plotted against Co, which better allows visualization of their variations (Fig. 10 and 11). This is because Co concentrations in Pn are the highest (around 1 %), followed by Po and Ccp, which show a small overlap mainly ranging from 5 to 100 ppm and 0.1 to 20 ppm, respectively. As indicated by the maps of element distributions, trace elements concentrations are highest in Pn. Pyrrhotite and Ccp contain from 200 to 1800 ppm and 5 to 200 ppm Ni, respectively (Fig. 10a). Apart from one sample, Pd is in the 20 to 400 ppm range for Pn, whereas Po and Ccp contain below 10 ppm (Fig. 10b). Rhodium and Ru vary mostly from 0.1 to 50 ppm in Pn and are below 5 ppm in Po (Fig. 10c and 10d). Chalcopyrite has very low Ru contents. Iridium and Os are distributed between Pn and Po and range from 0.01 to 5 ppm in the former and 0.01 to 1 ppm in the latter, with values for Ccp below detection limits (Fig. 10e and 10f). Platinum, Re, Mo, Bi, Sn, and Tl are distributed among Po, Pn, and Ccp but concentrations are mainly below 1 ppm (Fig. 10g to 10l). Tellurium and As show remarkably high concentrations in Pn, attaining 500 ppm (Fig. 10m and 10n), but values are variable, probably due to the observed frequent zonation patterns. Concentrations of both elements in Po and Ccp are below 10 ppm.

Copper median concentrations vary from 1 to 1000 ppm in both Po and Pn (Fig. 11a). Zinc contents are higher in Ccp, ranging from 100 to 5000 ppm, relative to Po and Pn where it varies mostly from 0.1 to 100 ppm (Fig. 11b). Indium and Cd are also higher in Ccp relative to Po and Pn, however, concentrations in all the BMS are below 10 ppm (Fig. 11c and 11d). Lead and Ag have similar concentrations in all sulfides but show a wide variation range, mostly from 0.01 to 50 ppm (Fig. 11e and 11f). Selenium is present in subequal amounts in all BMS, ranging from 50 to 300 ppm (Fig. 11g). Antimony concentrations are less than detection limit for most of the sulfides (<0.05 ppm), apart from a few analyses which attain 1 ppm (Fig. 11h).

Mass balance

The weight fraction of each element in each BMS was calculated to establish which mineral(s) host the bulk of each element in the Sulfide zone. The proportion of each element hosted in each BMS was calculated following the method used by Barnes *et al.* (2006). This calculation requires: (1) the concentration of each element in the whole rock (ESM – Table 4); (2) the median concentration of each element in each BMS (ESM – Tables 5–7); and (3) the weight fraction of each BMS. The weight fractions of Ccp, Po, and Pn were calculated using whole-rock Cu, Ni, and S and the concentrations of Cu and Ni in each mineral. The Cu was assigned to Ccp, whereas the Ni was assigned to Pn. The contributions of Ni from olivine and orthopyroxene were deducted prior to calculation of the weight fraction of Pn. The concentrations of Ni in olivine and orthopyroxene and the proportions of these minerals in each sample were reported by Mansur & Ferreira Filho (2016). The remaining S was attributed to Po.

The accumulated error of the different results used for the mass balance calculation is approximately 20% at one standard deviation (1σ). Therefore, a wide variation may occur when considering different samples because of different accumulated errors in LA-ICP-MS and whole-rock analyses, weight fractions of different mineral, and sample heterogeneities. In order to minimize these variations and obtain realistic mass balance calculations, a larger number of samples is required. We used nine different samples from the Sulfide zone in order to minimize the effects of different errors and natural variability and to calculate the mass balance for BMS in the deposit. In order for the readers to be able to assess the variability range of the calculations the minimum, maximum, and average results for mass balance calculations for Po, Pn, and Ccp are summarized in electronic supplementary materials (ESM – Table 8).

The summary of the mass balance average results is show in Figure 12. The BMS host most of Co, Ni, and Se (more than 50%), but lower amounts of As, Ru, Rh, Pd, Te, and Os (10 to 50%). Only negligible amounts (<5%) of Sb, Ir, Pt, Au, and Bi are hosted within the BMS. Pentlandite hosts virtually all of the Co, Ni, As, Ru, Rh, Pd, Te, and Os, whereas Se is evenly present in all BMS, and the main host is the most common mineral in each sample, normally Pn and Po. The small portion of Bi hosted by BMS is present within Po.

Discussion

The effect of crustal assimilation on high As contents in the Luanga deposit

One of the remarkable features observed at the Luanga deposit is the anomalously high As contents in BMS, especially in Pn. The distribution of As is not always homogeneous and frequently shows a core-to-rim decrease (Fig. 9). This zonation likely explains the wide range of concentrations found, but nevertheless, most of the Pn analyses yield from 50 to 500 ppm As (Fig. 10n). In comparison to Pn from other magmatic sulfide deposits worldwide, the As contents in the Pn from the Sulfide zone are among the highest values found to date (Fig. 13). It is also noteworthy that the literature results include localities such as the Rosie prospect (Godel *et al.* 2012) and the Creighton

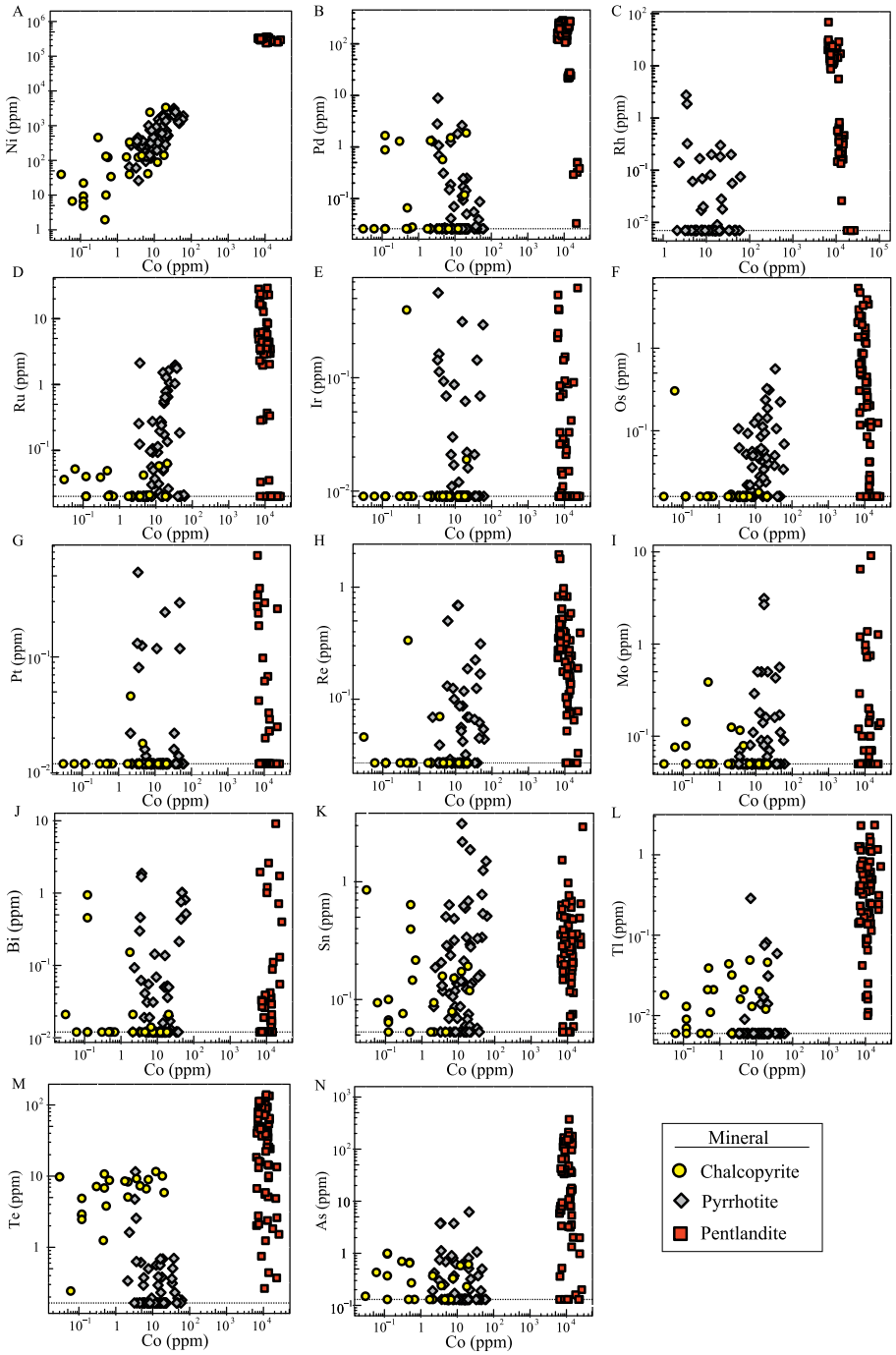

FIG. 10. Binary plots of (a) Ni, (b) Pd, (c) Rh, (d) Ru, (e) Ir, (f) Os, (g) Pt, (h) Re, (i) Mo, (j) Bi, (k) Sn, (l) Tl, (m) Te, and (n) As *versus* Co for pyrrhotite, pentlandite, and chalcopyrite from the Sulfide zone of the Luanga deposit. Dashed lines indicate the detection limits. The full LA-ICP-MS data set is given in the ESM, Tables 5–7.

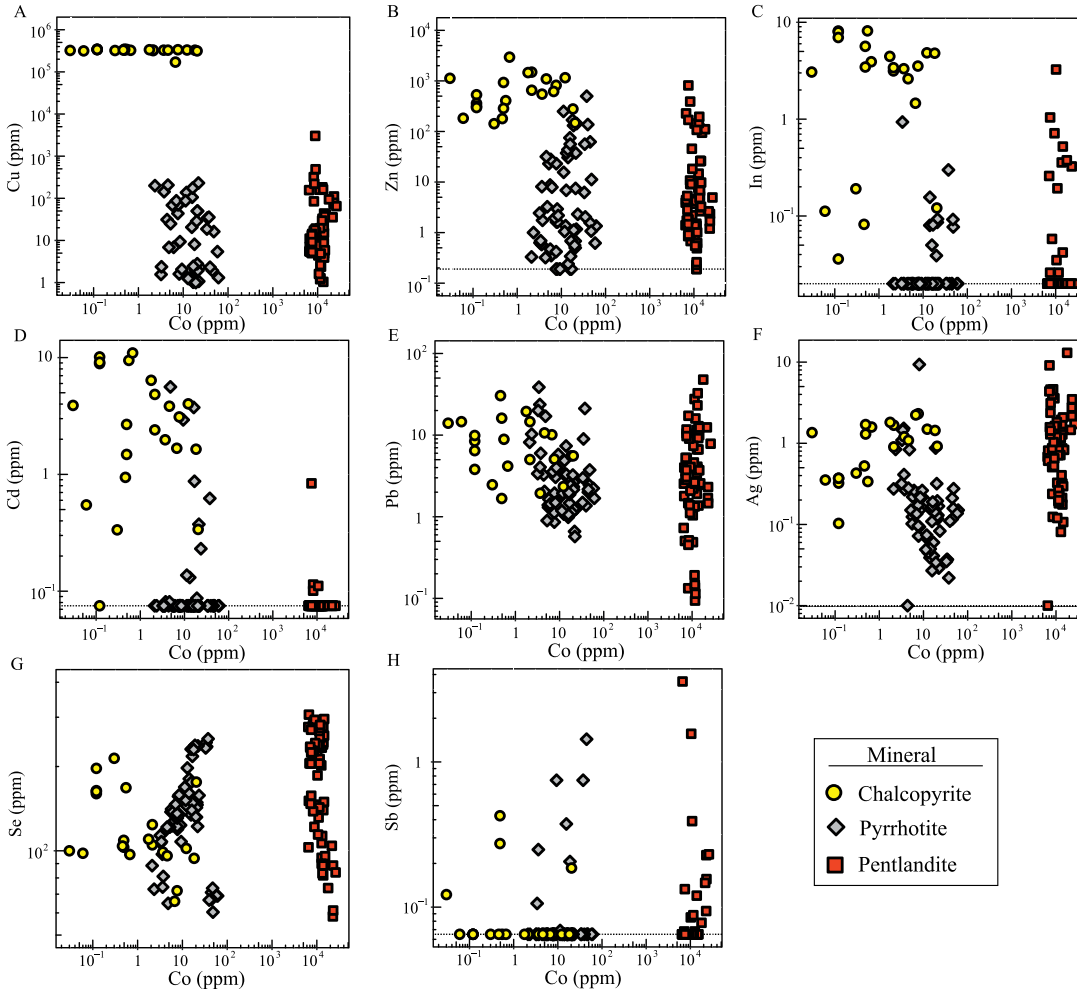

FIG. 11. Binary plots of (a) Cu, (b) Zn, (c) In, (d) Cd, (e) Pb, (f) Ag, (g) Se, and (h) Sb *versus* Co for pyrrhotite, pentlandite, and chalcopyrite from the Sulfide zone of the Luanga deposit. Dashed lines indicate the detection limits. The full LA-ICP-MS data set is given in the ESM, Tables 5–7.

deposit from the Sudbury Complex (Dare *et al*. 2010a, 2010b), where the initial magmas are interpreted to have become As-rich due to assimilation of country rock.

Given the only slightly chalcophile behavior of As (Liu & Brenan 2015, Barnes 2016, Maciag & Brenan 2020), high concentrations in the sulfide liquid cannot be achieved simply by interacting with large volumes of silicate magma (*i.e*., high *R*-factors; Mansur & Barnes 2020b). Instead, the silicate magma from which the immiscible sulfide liquid has segregated is required to have been relatively As-rich. However, As concentrations in basaltic magmas are very low (Jenner & O'Neill 2012). Continental crustal assimilation could be responsible for upgrading the As contents in the magmas, particularly in cases where black shales were the contaminants (Dare *et al*. 2010a, Godel *et al*. 2012, Piña *et al*. 2015, Duran *et al*. 2017, Knight *et al*. 2017, Samalens *et al*. 2017b, Le Vaillant *et al*. 2018, Mansur & Barnes 2020b). Therefore, the high As contents found in sulfides from the Luanga deposit could be explained by the assimilation of As-rich country rocks. However, prior to considering the role of crustal assimilation one should first assess the amount of As in the initial magma that would be required to produce the concentrations found in the sulfides from the Luanga deposit.

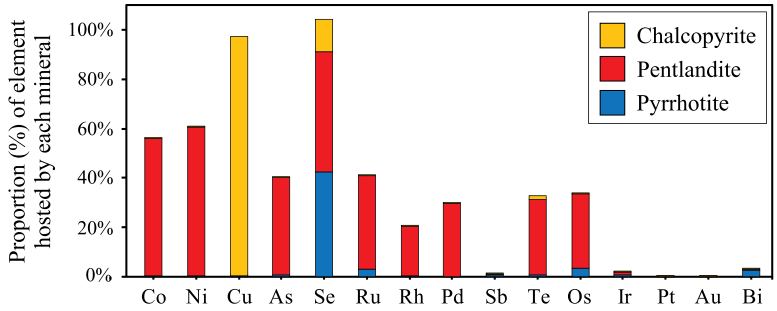

FIG. 12. Average proportion (%) of each element hosted in pyrrhotite, pentlandite, and chalcopyrite from the Sulfide zone of the Luanga deposit. The minimum, maximum, and average results for mass balance calculations are summarized in the electronic supplementary materials (ESM – Table 8).

We used the average whole-rock concentrations of TABS+ in the Sulfide zone and their different partition coefficients into an immiscible sulfide liquid to estimate their concentrations in the silicate liquid from which the deposit formed. We also included Pd as a proxy for PGE to assure that the parameters are appropriate for elements with very variable partition coefficients. The composition of the sulfide liquid was

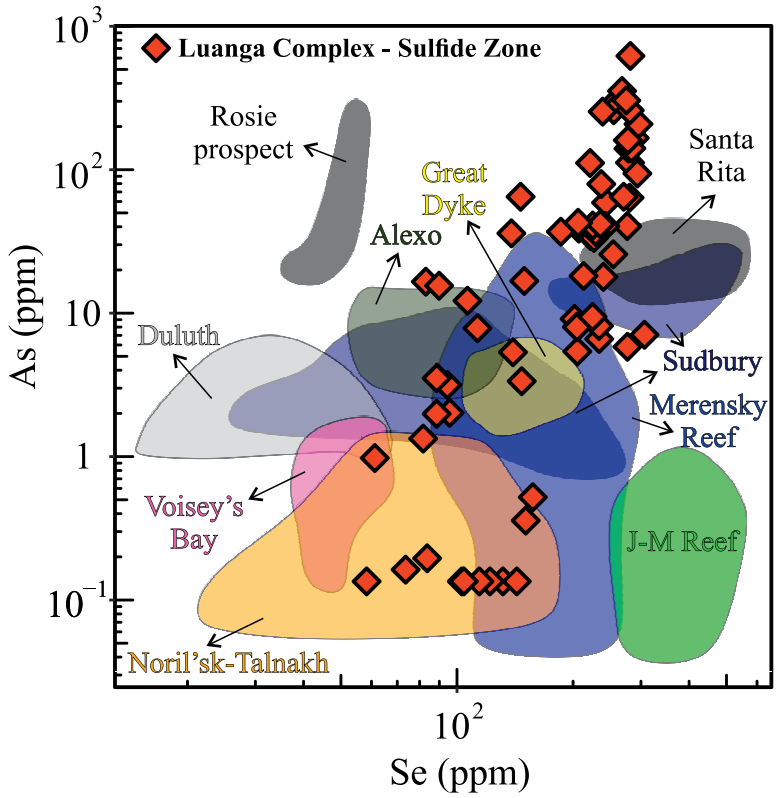

FIG. 13. Binary plot of As *versus* Se in pentlandite from samples of the Sulfide zone of the Luanga deposit. The compositional fields for pentlandite from other magmatic sulfide deposits presented by Mansur *et al.* (2020d) are shown for comparison. Note that As concentrations in pentlandite from the Luanga deposit are among the highest values found to date. Please see text for further explanation.

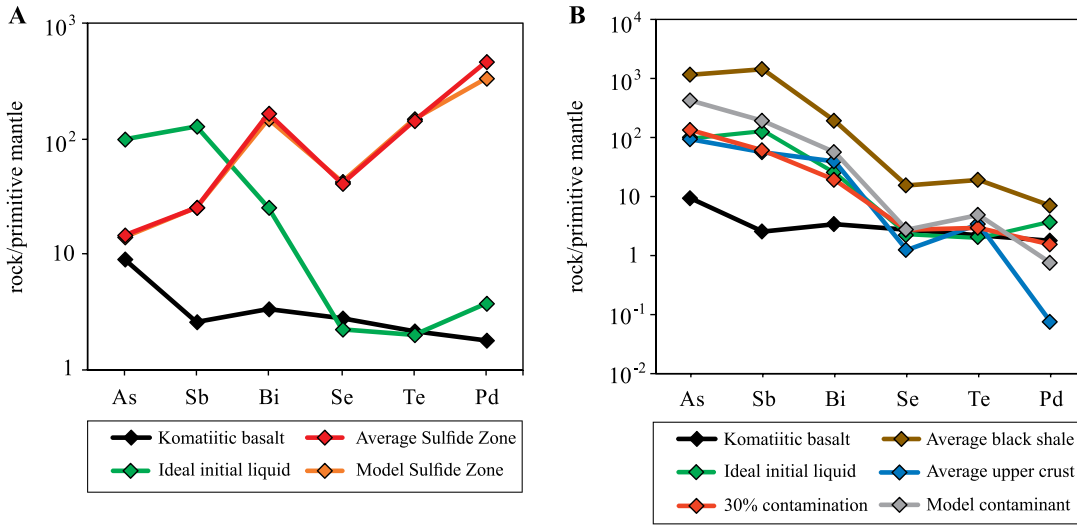

FIG. 14. Mantle-normalized TABS-Pd diagrams for (a) average composition of the Sulfide zone, komatiitic basalt (Barnes 2016), calculated composition of an ideal liquid for the crystallization of the Sulfide zone, and the calculated composition of the Sulfide zone crystallized from this ideal liquid; (b) komatiitic basalt (Barnes 2016), upper continental crust (Hu & Gao 2008), black shale (Ketris & Yudovich 2009), calculated composition of an ideal liquid for the crystallization of the Sulfide zone, a contaminant consisting of a 70:30 mixture of upper continental crust and black shale, and the calculated product of 30% assimilation of this contaminant by a komatiitic basalt. Primitive mantle values from Lyubetskaya & Korenaga (2007).

modeled using the equation of Campbell & Naldrett (1979):

$$C_{\mathrm{Sul}} = C_{\mathrm{Sil}} D^{\mathrm{Sul/Sil}} (R+1) \Big/ \left(R + D^{\mathrm{Sul/Sil}}\right) \qquad (1)$$

where C_{Sul} is the concentration of an element in the sulfide liquid, C_{Sil} is the concentration of an element in the silicate liquid, $D^{\mathrm{Sul/Sil}}$ is the partition coefficient for the element between sulfide and silicate liquid, and R is the ratio of silicate to sulfide liquid. The utilized partition coefficients were 2, 5, 500, 1200, 3000, and 40,000 for As, Sb, Bi, Se, Te, and Pd, respectively (Mungall & Brenan 2014, Li & Audétat 2015, Liu & Brenan 2015), and the R-factor around 14,000. The cumulate sulfide liquid fraction was estimated by

$$\mathrm{wt.\%.\ sulf} = \mathrm{S\ rock}/350000 \qquad (2)$$

assuming that sulfide liquid contained approximately 35 wt.% S.

The obtained results are shown in the mantle-normalized plot in Figure 14. The concentrations of Se, Te, and Pd in the Sulfide zone can be modeled using the aforementioned parameters and would require a silicate liquid with a composition resembling a komatiitic basalt (Barnes 2016). Indeed, Mansur & Ferreira Filho (2016) investigated the cryptic variations in olivine and orthopyroxene across the stratigraphy of the Luanga Complex and argued that high forsterite and enstatite contents (*i.e.*, Fo_{80}–Fo_{87} and En_{75}–En_{90}) support a primitive parental magma for the Luanga Complex. This is also supported by the high Ni concentrations in both minerals (*e.g.*, 3500 to 6000 ppm in olivine and 800 to 1600 ppm in orthopyroxene) reported by Mansur & Ferreira Filho (2016). However, the concentrations of As, Sb, and Bi found in average komatiitic basalts are much lower than required for the formation of the Sulfide zone (Fig. 14a), thus supporting their external addition by crustal assimilation prior to the formation of the deposit.

The mantle-normalized pattern for the silicate liquid required to form the Sulfide zone resembles the average upper continental crust (Hu & Gao 2008; Fig. 14b). Also, the pattern is similar to those obtained for the B-1 magmas that formed the Bushveld Complex, which are assumed to have undergone ~20 to 40% of crustal assimilation (Barnes *et al.* 2010, Wilson 2012, Maier *et al.* 2016, Mansur & Barnes 2020b). However, the concentrations of As, Sb, and Bi in the required silicate liquid for the Luanga deposit require a much richer contaminant than upper continental crust. A possible contaminant are black shales, which occur in the eastern portion of the Carajás Mineral Province (CMP) (Cabral *et al.* 2013, Tavares *et al.* 2018). We calculated a contaminant comprising a mixture of 70% upper continental crust and 30% average black shales (Ketris & Yudovich

2009). The patterns for the silicate liquid required to form the Sulfide zone can be reproduced by mixing an initial komatiitic basalt with approximately 30% of this contaminant (Fig. 14b).

Overall, the modeling results support the idea that high concentrations of not only As, but also to a lesser extent Sb and Bi, found in the Luanga deposit can be explained by assimilation of a mixture of upper continental crust and black shales by a primitive komatiitic basalt (Fig. 14b). Indeed, the whole-rock geochemistry of lithophile elements in rocks from the Luanga Complex also supports the assimilation of crustal-derived material during the evolution of the intrusion (Mansur & Ferreira Filho 2016). Geochemical signatures supporting the assimilation of crustal material during evolution were also observed in other layered intrusions located in the eastern portion of the CMP (Teixeira *et al*. 2015). Our results show that crustal assimilation is an important process allowing for the upgrade of concentrations of slightly chalcophile elements in mantle-derived magmas.

The formation of the low-S-high-PGE zone and the role of TABS+ during post-cumulus alteration

Most of the global PGE resources are hosted within magmatic deposits subdivided into sulfide- and chromite-related, as exemplified by the world-class PGE deposits of the Merensky Reef and UG-2 chromitite, from the Bushveld Complex (*e.g*., Barnes & Maier 2002, Cawthorn *et al*. 2002, Maier 2005, Cawthorn 2015). The common processes that lead to PGE concentration are the segregation of an immiscible sulfide liquid (*e.g*., Naldrett 2004, Mungall & Naldrett 2008) and crystallization of chromite crystals (*e.g*., Finnigan *et al*. 2008). However, several studies have also highlighted the presence of PGE-mineralized rocks devoid of chromite and sulfides, which are commonly referred to as low-S ores (Kaukonen 2008, Sluzhenikin *et al*. 2014, 2020, Tuba *et al*. 2014, Maier *et al*. 2015, Barnes *et al*. 2016, Tanner *et al*. 2019, Mansur *et al*. 2020b). Some of these occurrences are hosted within evolved rocks in the upper parts of layered intrusions, normally associated with oxides (*e.g*., Skaergaard Intrusion – Holwell & Keays 2014, Stella intrusion – Maier *et al*. 2003), whereas others are hosted in less-evolved portions of the intrusions and have no indicator minerals (*e.g*., Lac des Iles, High-grade zone – Hinchey & Hattori 2005, Djon & Barnes 2012; Jinbaoshan deposit – Wang *et al*. 2008). The low-S-high-PGE zone found at the Luanga deposit is an example of this low-S class of PGE mineralization hosted within less evolved rocks and devoid of indicator minerals and allows for better understanding of their formation and also the roles of TABS+ for PGE collection.

A genetic model for the formation of the low-S-high-PGE zone must take into account: (1) similar degrees of alteration observed in these rocks and the Sulfide zone, (2) different Pt/Pd ratios, (3) whole-rock contents of TABS+, and (4) PGM assemblages observed in both PGE-rich zones. These variations are considered below, and we explore the hypotheses of direct crystallization of PGM from the silicate magma and post-cumulus alteration as mechanisms for the formation of the low-S-high-PGE zone.

A proposed model for the origin of low-S-high-PGE ores is the direct crystallization of PGM from the silicate magma. This model explains the presence of Pt-arsenides in S-undersaturated rocks from the Monts de Cristal Complex (Maier *et al*. 2015, Barnes *et al*. 2016). The model has also found support from a number of experimental (Helmy *et al*. 2013, 2020, Helmy & Bragagni 2017, Anenburg & Mavrogenes 2020) and observational studies (Wirth *et al*. 2013, Junge *et al*. 2015, Kamenetsky *et al*. 2015, González-Jiménez & Reich 2017, González-Jiménez *et al*. 2018, 2019, Liang *et al*. 2019, Kamenetsky & Zelenski 2020) which report the presence of nanometer-sized particles, comprising mainly a combination of PGE and TABS+, in silicate magmas (*e.g*., Tredoux *et al*. 1995). However, one of the limiting factors for the direct crystallization of PGM from a silicate magma is that extensive external addition of TABS+ would be required in order to attain PGE-TABS+ saturation (Canali *et al*. 2017). In the case of the Luanga deposit this would likely not represent a limiting factor, as high As (and also Sb and Bi) contents are argued to result from crustal assimilation (Fig. 14). However, although similar As concentrations are found in both mineralization styles, a very large proportion of the As is found within BMS structures in the Sulfide zone (Figs. 9 and 12). Therefore, it seems counterintuitive that direct crystallization of Pt-arsenides from the silicate liquid was the main mechanism leading to the formation of low-S-high-PGE zone. Moreover, this mechanism would also require the magma to become saturated in Pd, which has a higher solubility in the silicate magma (Brenan *et al*. 2016 and references therein), thus not favoring this hypothesis.

Another possible mechanism leading to the formation of the low-S-high-PGE zone is post-cumulus alteration. In this case, the PGE-rich intervals would have formed by the segregation and accumulation of an immiscible sulfide liquid followed by the loss of S during further alteration (Li *et al*. 2004, Polovina *et al*. 2004, Godel & Barnes 2008, Kawohl & Frimmel 2016, Mansur *et al*. 2020b). This process is supported by low S/Se ratios (Queffurus & Barnes 2015), and also the

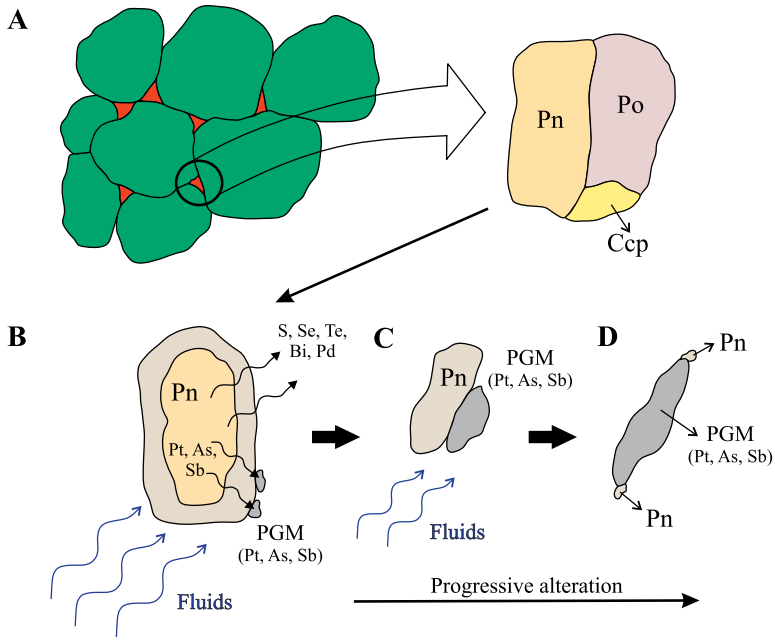

FIG. 15. Schematic models illustrating the formation of the low-S-high-PGE zone by S loss from magmatic sulfides. Note that a portion of Se, Te, Bi, and Pd are lost together with S, whereas As and Sb are expelled from the sulfide lattice and combine with PGE (mostly Pt) to form PGM. See text for further explanation. Po: pyrrhotite; Pn: pentlandite; Ccp: chalcopyrite; PGM: platinum-group minerals.

variable degree of alteration observed in the BMS from the Sulfide zone, and pervasive secondary alteration observed in the rocks from the low-S-high-PGE zone. However, constraining whether the nature of the altering fluids is hydro-magmatic or metamorphic is not straightforward in the case of the Luanga deposit using our results. It is noteworthy that there is no significant difference in the degree of alteration of silicate minerals in rocks from both the low-S-high-PGE and the Sulfide zones (Mansur & Ferreira Filho 2016, Mansur *et al*. 2020b). This suggests that the alteration was pervasive through the Luanga Complex as a whole, equally affecting most lithologies and not constrained to specific horizons. Although this remains a hypothesis to be further tested, a metamorphic event would likely affect the intrusion in a more homogenous manner relative to a hydro-magmatic event. We do not rule out any possibility but considering the homogeneous nature of the alteration affecting the Luanga Complex, a metamorphic event seems to be a more plausible alternative at this stage.

Although the post-cumulus alteration observed in the Luanga Complex does not vary for different portions of the intrusion, some factor is required to account for the better preservation of BMS in the Sulfide zone relative to the low-S-high-PGE zone. Several alteration features are observed in the Sulfide zone including the intergrowth of secondary silicates and BMS (Fig. 3b), the presence of magnetite rims around sulfide droplets (Fig. 3b), and lower concentrations of chalcophile elements at BMS grain boundaries (Fig. 9). It is possible that the Sulfide zone had initially larger volumes of sulfides relative to the low-S-high-PGE zone, and these could have diminished the effects of alteration by diminishing the available alteration surface in the sulfides. This would also be in agreement with the higher PGE contents found in the Sulfide zone, supporting a more extensive sulfide accumulation. Alternatively, it could also be possible that greater volumes of fluids were present at higher stratigraphic horizons of the intrusions and could have led to a more ready alteration of the BMS from the low-S-high-PGE zone. Our results do not distinguish between these hypotheses.

Given that the low-S-high-PGE zone likely formed by post-cumulus alteration, it is possible to constrain its effect on the distribution of TABS+ (Fig. 15a). The low-S-high-PGE and Sulfide zones have comparable contents of As and Sb, but the former has significantly lower Te, Bi, and Se contents than the latter. This suggests that the progressive alteration and S loss also led to the loss of Te, Bi, and some Se (Fig. 15b). Our

results also support the suggestion that a portion of the Pd was lost during alteration, thus leading to higher Pt/Pd ratios in the low-S-high-PGE zone. This interpretation is also supported by the variable PGM mineralogy and the whole-rock distribution of TABS+ in both zones (Figs. 4 and 7i to k). Similar findings are also reported for the SJ Reef of the Penikat intrusion, in which the presence of Pt-arsenides is argued to result from S loss (Kaukonen 2008). A comparable process is also argued for the formation of low-sulfide PGE ores of the Noril'sk-Talnakh Camp (Sluzhenikin *et al*. 2014, 2020), interpreted to have formed by S loss. However, in this case the S loss, potentially accompanied by other metals, was due to degassing at low eruptive pressures.

Our results suggest that TABS+ may play a role during the alteration of magmatic sulfide deposits. Zonation profiles observed in BMS from the Sulfide zone support the progressive loss of Se, Te, and As at grain boundaries (Fig. 9). It is possible that these elements were expelled from BMS lattices upon alteration and may have combined with PGE to form PGM (Fig. 15b to 15d). However, TABS+ form PGM that are stable at different conditions. For example, As and Sb are more frequently associated with Pt, and form PGM that are stable at higher temperatures (Bennett & Heyding 1966, Dare *et al*. 2010a, Helmy *et al*. 2013, Bai *et al*. 2017). In contrast, Te and Bi are frequently combined with Pd and form PGM that have lower melting temperatures (Cabri & Laflamme 1976, Hoffman & MacLean 1976, Helmy *et al*. 2007, Tomkins *et al*. 2007, Dare *et al*. 2014, Duran *et al*. 2017, Mansur *et al*. 2020a). Consequently, it is expected that Te, Bi, and Pd could be more readily remobilized relative to Pt, As, and Sb. The preferential remobilization of Pd relative to Pt is supported by other studies (Godel & Barnes 2008, Holwell *et al*. 2017, van den Kerkhof *et al*. 2018, Oberthur *et al*. 2018). Moreover, the preferential remobilization of Te, Se, and Bi from magmatic sulfides by late fluids was argued by Dare *et al*. (2014) to have occurred in Cu-rich ores of the McCreedy East deposit, Sudbury, and is progressively gaining more attention in recent contributions (Howell *et al*. 2019, Blanks *et al*. 2020). We suggest that As and Sb may act as fixing agents for PGE (especially Pt) during post-cumulus alteration, in a model similar to that proposed by Wood (2002). This is also supported by high As concentrations in Pn from the Sulfide zone, which during alteration could have been expelled and made available for combination with PGE (mainly Pt), and form PGM. In contrast, Te, Bi, Se, and Pd are more easily remobilized, which could result in these elements being more readily available to post-cumulus fluids.

Although the BMS from the Luanga deposit show signs of post-cumulus alteration, their compositions are still comparable to those from unaltered magmatic sulfide deposits worldwide. Our results are plotted in discriminant diagrams available in the literature for separating BMS from magmatic and hydrothermal deposits (Duran *et al*. 2019, Mansur *et al*. 2020d), and also Ni-Cu and PGE-dominated deposits (Duran *et al*. 2015, Mansur *et al*. 2020d). Most of the Pn (Fig. 16a) and Ccp (Fig. 16b) analyses from the Sulfide zone fall within the fields for a magmatic PGE-dominated deposit. This supports the use of the discriminant diagrams for indicator minerals in situations where the source rocks may have undergone some form of post-cumulus alteration.

The potential link between magmatic and hydrothermal deposits in the Carajás Mineral Province

One of the main reasons why the CMP has been the focus of several studies over the past decades is the vast presence of mineral deposits. The province hosts a wide variety of deposit types (*e.g*., Ni, PGE, Mn, Cu-Au, among others; Monteiro *et al*. 2014), including the largest iron resources in the world (Klein & Ladeira 2002, Lobato *et al*. 2005, Figueiredo e Silva *et al*. 2013). Apart from these resources, the CMP also hosts a great number of IOCG deposits, which are likely to record several magmatic-hydrothermal episodes on a regional scale (Monteiro *et al*. 2008, Moreto *et al*. 2011, 2015, Xavier *et al*. 2012). These deposits have recently been interpreted as a continuum from different crustal depths (Schutesky & de Oliveira 2020), and variations in the metallogenetic association from each deposit may reflect different sources (Xavier *et al*. 2008, Torresi *et al*. 2012, Craveiro *et al*. 2019, de Melo *et al*. 2019, Garcia *et al*. 2020, Veloso *et al*. 2020). Our findings may contribute to understanding the sources of metals for at least some of the hydrothermal deposits found in the CMP. Moreover, the implications may also be applicable to the remobilization of some elements in magmatic-hydrothermal systems elsewhere.

Some of the deposits considered as part of the IOCG system from the CMP show Ni-rich zones, such as the Castanha and Jatobá deposits (Pestilho *et al*. 2020, Veloso *et al*. 2020), located in the southern portion of the province (Fig. 1). Moreover, hydrothermal Ni deposits with similar ages and alteration assemblages such as the GT-34 and the Jaguar deposits have been interpreted as members of the IOCG system of the CMP (Oliveira 2017, Garcia *et al*. 2020). For instance, the presence of magnetite-rich ore bodies within these hydrothermal Ni deposits have led some

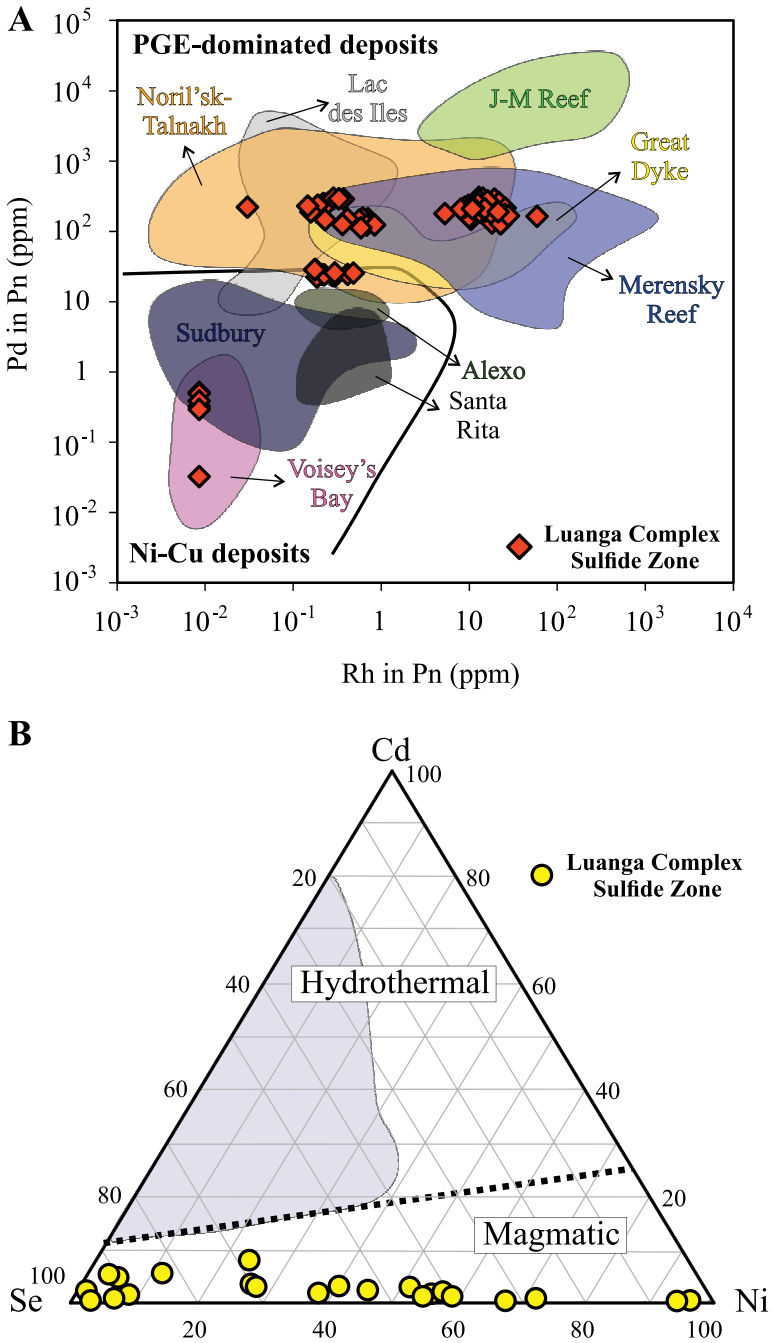

FIG. 16. Discriminant diagrams developed for the use of BMS as indicator minerals. (A) Binary plot of Pd *versus* Rh in pentlandite (Pn) for separating magmatic Ni-Cu and PGE-dominated deposits (Duran *et al*. 2015, Mansur *et al*. 2020d). (B) Ternary plot of Se, Cd, and Ni in chalcopyrite for separating magmatic and hydrothermal deposits (Duran *et al*. 2019). See text for further explanation. The compositional fields for pentlandite and chalcopyrite from magmatic deposits are given by Mansur *et al*. (2020d), whereas the field for chalcopyrite from hydrothermal deposits is reported by George *et al*. (2018).

authors to suggest that they may represent deeper portions of the IOCG system (Garcia *et al*. 2020, Schutesky & Oliveira 2020), as discussed for other regions (Dare *et al*. 2015, Knipping *et al*. 2015, Simon *et al*. 2018, Huang & Beaudoin 2019, La Cruz *et al*. 2020). It is also noteworthy that the BMS assemblage found in these hydrothermal Ni deposits is very similar to that found in magmatic sulfide deposits, comprising Po, Pn, and minor Ccp (Oliveira 2017, Garcia *et al*. 2020). Moreover, Garcia *et al*. (2020) also point out the presence of Pn exsolution lamellae within Po grains in the GT-34 deposits, a very typical feature observed in magmatic Ni-Cu deposits (Barnes & Lightfoot 2005, and references therein). Therefore, the similarities in mineral assemblages and the spatial relationship between magmatic and hydrothermal deposits within the CMP may raise the question of a genetic link between them.

Our results support the remobilization of S, Se, Te, Bi, and Pd from the Luanga deposit (Fig. 15). Thus, it is possible that the alteration of magmatic sulfide deposits hosted within the several layered intrusions found within the CMP (Ferreira Filho *et al*. 2007) may have led, at least at some localities, to the origin of Ni-rich zone within the IOCG system of the province. For example, Garcia *et al*. (2020) and Oliveira (2017) report Te enrichments in the ores from the GT-34 and Jaguar deposits, respectively. Thus, some of the elements that have been shown to be remobilized from magmatic sulfide deposits (*e.g*., Se, Te, Bi, Pd) may be used to track the link between magmatic and hydrothermal Ni deposits in the CMP. This is also in agreement with previous studies of hydrothermal Ni deposits arguing for a potentially magmatic sulfide deposit as the Ni source (González-Álvarez *et al*. 2013, Le Vaillant *et al*. 2015, 2016, Holwell *et al*. 2017), and also experiments supporting Ni transport in hydrothermal fluids (Liu *et al*. 2012, Tian *et al*. 2012, Scholten *et al*. 2018). We suggest that the alteration of magmatic sulfide deposits represents the source of the Ni found in some portions of the regional IOCG system in the CMP, and elements such as Se, Te, Bi, and Pd could be used to track this process and test this hypothesis.

Conclusions

We have measured the concentrations of S, PGE, and TABS+ in rocks from both PGE mineralization styles found in the Luanga deposit and the concentration of trace elements in BMS from the Sulfide zone. Our main findings are summarized as follows:

(1) The Luanga deposit hosts two different styles of PGE mineralization with distinct geochemical characteristics, referred to as the Sulfide zone and the low-S-high-PGE zone.
(2) The Sulfide zone has higher Pd, Se, Te, and Bi concentrations but similar As, Sb, and Pt concentrations than the low-S-high-PGE zone. This is reflected in the PGM assemblage, which is dominated by bismuthotellurides in the Sulfide zone and consists mainly of arsenides and antimonides in the low-S-high-PGE zone.
(3) In the Sulfide zone, most of the Co, Ni, Cu, and Se, but only around 20 to 50 % of Pd, Rh, Os, Te, and As whole-rock budget is accounted for by the BMS. In many cases the BMS, especially Pn, display zonation patterns with As, Te, Se, and IPGE concentrations decreasing from core to borders, suggesting the loss of these elements in the outer portions of the crystals.
(4) The Pn from the Sulfide zone have anomalously high As contents (50 to 500 ppm), which would require the sulfides to have segregated from a very As-rich silicate magma. Considering an average komatiitic basalt as the parental magma, around 30% assimilation of a contaminant consisting of a mixture of approximately 70% upper continental crust and 30% black shales would be required.
(5) The low-S-high-PGE zone formed by S-loss from magmatic sulfides during post-cumulus alteration of the Luanga Complex. A portion of Se, Te, Bi, and Pd was also lost together with S, likely making these elements available for remobilization by hydrothermal fluids. In contrast, As and Sb were expelled from BMS structures and combined with PGE to form PGM, suggesting they may play a role fixing PGE during alteration.
(6) The alteration of magmatic sulfide deposits hosted within layered intrusions from the CMP may be genetically linked to the formation of hydrothermal Ni deposits as part of the IOCG system of the province. The concentrations of elements remobilized from the magmatic sulfide deposits (*e.g*., Se, Te, Bi, Pd) may be used to investigate this process.

Acknowledgments

This work was supported by a Canada Research Chair program grant (215503) and a Discovery Grant (1884-2013) to Sarah-Jane Barnes. Cesar F. Ferreira Filho is a Research Fellow at CNPq (Conselho Nacional de Desenvolvimento Científico e Tecnológico - Processo 302465/2019-7) and acknowledges the continuous support by the Coordenação de Aperfeiçoamento de Pessoal de Nível Superior - Brasil (CAPES) - Finance Code 001. This manuscript benefited from insightful comments from the reviewers Belinda Godel and Rubén Piña, and careful

editorial handling by the editors Malte Junge and Lee Groat.

References

Andersen, J.C. (2006) Postmagmatic sulphur loss in the Skaergaard intrusion: implications for the formation of the Platinova Reef. *Lithos* **92(1–2)**, 198–221.

Anenburg, M. & Mavrogenes, J.A. (2020) Noble metal nanonugget insolubility in geological sulfide liquids. *Geology* **48 (9)**, 939–943.

Bai, L., Barnes, S.J., & Baker, D.R. (2017) Sperrylite saturation in magmatic sulfide melts: Implications for formation of PGE-bearing arsenides and sulfarsenides. *American Mineralogist* **102(5)** 966–974.

Barnes, S-J. (2016) Chalcophile elements. *In* Encyclopedia of Geochemistry: A Comprehensive Reference Source on the Chemistry of the Earth (W.M. White, ed.). Springer International Publishing. (1–5).

Barnes, S-.J. & Lightfoot, P.C. (2005) Formation of magmatic nickel sulfide deposits and processes affecting their copper and platinum group element contents. *Economic Geology 100th Anniversary Volume* 179–214.

Barnes, S.-J. & Maier, W.D. (2002) Platinum-group elements and microstructures of Normal Merensky Reef from Impala Platinum Mines, Bushveld Complex. *Journal of Petrology* **43(1)**, 103–128.

Barnes, S.-J. & Mansur, E.T. (in press) Processes affecting the distribution of Te, As, Bi, Sb and Se (TABS+) in: picrites and basalts from large igneous provinces; MORB, and komatiites as illustrated by bulk silicate earth plots. *Economic Geology*, in press.

Barnes, S-J. & Ripley, E.M. (2016) Highly siderophile and strongly chalcophile elements in magmatic ore deposits. *Reviews in Mineralogy and Geochemistry* **81**, 725–774.

Barnes, S-J., Cox, R., & Zientek, M. (2006) Platinum-group element, gold, silver and base metal distribution in compositionally zoned sulfide droplets from the Medvezky Creek Mine, Noril'sk, Russia. *Contribution to Mineralogy and Petrology* **152**, 187–200.

Barnes, S-J., Prichard, H.M., Cox, R.A., Fisher, P.C., & Godel, B. (2008) The location of the chalcophile and siderophile elements in platinum-group element ore deposits (a textural, microbeam and whole rock geochemical study): Implications for the formation of the deposits. *Chemical Geology* **248**, 295–317.

Barnes, S-J., Savard, D., Bédard, L.P., & Maier, W.D. (2009) Selenium and sulfur concentrations in the Bushveld Complex of South Africa and implications for formation of the platinum-group element deposits. *Mineralium Deposita* **44(6)**, 647–663.

Barnes, S.-J., Maier, W.D., & Curl, E.A. (2010) Composition of the marginal rocks and sills of the Rustenburg Layered Suite, Bushveld Complex, South Africa: Implications for the formation of the platinum-group element deposits. *Economic Geology* **105(8)**, 1491–1511.

Barnes, S.J., Fisher, L.A., Godel, B., Maier, W.D., Paterson, D., Howard, D.L., Ran, C.G., Laird, J.S., & Pearce, M.A. (2016) Primary cumulus platinum minerals in the Monts de Cristal Complex, Gabon: magmatic microenvironments inferred from high-resolution X-ray fluorescence microscopy. *Contributions to Mineralogy and Petrology* **171(3)**, 1–18.

Barnes, S.J., Holwell, D.A., & Le Vaillant, M. (2017) Magmatic sulfide ore deposits. *Elements* **13(2)**, 89–95.

Barnes, S.J., Taranovic, V., Schoneveld, L.E., Mansur, E.T., Le Vaillant, M., Dare, S., Staude, S., Evans, N.J., & Blanks, D. (2020) The occurrence and origin of pentlandite-chalcopyrite-pyrrhotite loop textures in magmatic Ni-Cu sulfide ores. *Economic Geology* **115(8)**, 1777–1798.

Bédard, L.P., Savard, D., & Barnes, S-J. (2008) Total sulfur concentration in geological reference materials by elemental infrared analyser. *Geostandards and Geoanalytical Research* **32(2)**, 203–208.

Bennett, S.L. & Heyding, R.D. (1966) Arsenides of the transition metals. VIII. Some binary and ternary group VIII diarsenides and their magnetite and electric properties. *Canadian Journal of Chemistry* **44**, 3017–3030.

Blanks, D.E., Holwell, D.A., Fiorentini, M.L., Moroni, M., Giuliani, A., Tassara, S., & Ferrari, E. (2020) Fluxing of mantle carbon as a physical agent for metallogenic fertilization of the crust. *Nature Communications* **11(1)**, 1–11.

Brenan, J.M., Bennett, N.R., & Zajacz, Z. (2016) Experimental results on fractionation of the highly siderophile elements (HSE) at variable pressures and temperatures during planetary and magmatic differentiation. *Reviews in Mineralogy and Geochemistry* **81(1)**, 1–87.

Brzozowski, M.J., Samson, I.M., Gagnon, J.E., Good, D.J., & Linnen, R.L. (2020) On the mechanisms for low-sulfide, high-platinum group element and high-sulfide, low-platinum group element mineralization in the eastern gabbro, Coldwell Complex, Canada: evidence from textural associations, S/Se values, and platinum group element concentrations of base metal sulfides. *Economic Geology* **115(2)**, 355–384.

Cabral, A.R., Creaser, R.A., Nägler, T., Lehmann, B., Voegelin, A.R., Belyatsky, B., Pasava, J., Seabra Gomes, A.A., Jr., Galbiatti, H., Boettcher, M.E., & Escher, P. (2013). Trace-element and multi-isotope geochemistry of Late-Archean black shales in the Carajás iron-ore district, Brazil. *Chemical Geology* **362**, 91–104.

Cabri, L.J. & Laflamme, J.H.G. (1976) The mineralogy of the platinum-group elements from some copper-nickel deposits of the Sudbury area, Ontario. *Economic Geology* **71**, 1159–1195.

Campbell, I.H. & Naldrett, A.J. (1979) The influence of silicate: Sulfide ratios on the geochemistry of magmatic sulfides. *Economic Geology* **74(6)**, 1503–1506.

Canali, A.C., Brenan, J.M., & Sullivan, N.A. (2017) Solubility of platinum-arsenide melt and sperrylite in synthetic basalt at 0.1 MPa and 1200° C with implications for arsenic speciation and platinum sequestration in mafic igneous systems. *Geochimica et Cosmochimica Acta* **216**, 153–168.

Cawthorn, R.G. (2015) The Bushveld complex, South Africa. *In* Layered Intrusions (B. Charlier, O. Namur, R. Latypov, & C. Tegner, eds.). Springer, Dordrecht, Netherlands (517–587).

Cawthorn, R.G., Merkle, R.K.W., & Viljoen, M.J. (2002) Platinum-group element deposits in the Bushveld Complex, South Africa. *In* The Geology, Geochemistry, Mineralogy and Mineral Beneficiation of Platinum-Group Elements (L.J. Cabri, ed.). *Canadian Institute of Mining, Metallurgy and Petroleum Special Volume* **54**, 389–430.

Craveiro, G.S., Villas, R.N.N., & Xavier, R.P. (2019) Mineral chemistry and geothermometry of alteration zone in the IOCG Cristalino deposit, Carajás Mineral Province, Brazil. *Journal of South American Earth Sciences* **92**, 481–505.

Dardenne, M.A. & Schobbenhaus, C.S. (2001) *Metalogênese do Brasil*. Brasília, UnBCNPq, pp. 392 (in Portuguese).

Dare, S.A.S., Barnes, S-J., Prichard, H.M., & Fisher, P.C. (2010a) The timing and formation of platinum-group minerals from the Creighton Ni-Cu-platinum-group element sulfide deposit, Sudbury, Canada: Early crystallization of PGE-rich sulfarsenides. *Economic Geology* **105**, 1071–1096.

Dare, S.A.S., Barnes, S-J., & Prichard, H.M. (2010b) The distribution of platinum group elements (PGE) and other chalcophile elements among sulfides from the Creighton Ni–Cu–PGE sulfide deposit, Sudbury, Canada, and the origin of palladium in pentlandite. *Minerlium Deposita* **45**, 765–793.

Dare, S.A.S., Barnes, S-J., Prichard, H.M., & Fisher, P.C. (2011) Chalcophile and platinum-group element (PGE) concentrations in the sulfide minerals from the McCreedy East deposit, Sudbury, Canada, and the origin of PGE in pyrite. *Mineralium Deposita* **46(4)**, 381–407.

Dare, S.A.S., Barnes, S-J., Prichard, H.M., & Fisher, P.C. (2014) Mineralogy and geochemistry of Cu-rich ores from the McCreedy East Ni-Cu-PGE deposit (Sudbury, Canada): Implications for the behavior of platinum group and chalcophile elements at the end of crystallization of a sulfide liquid. *Economic Geology* **109**, 343–366.

Dare, S.A., Barnes, S.J., & Beaudoin, G. (2015) Did the massive magnetite "lava flows" of El Laco (Chile) form by magmatic or hydrothermal processes? New constraints from magnetite composition by LA-ICP-MS. *Mineralium Deposita* **50(5)**, 607–617.

de Melo, G.H., Monteiro, L.V., Xavier, R.P., Moreto, C.P., & Santiago, E. (2019) Tracing Fluid Sources for the Salobo and Igarapé Bahia Deposits: Implications for the Genesis of the Iron Oxide Copper-Gold Deposits in the Carajás Province, Brazil. *Economic Geology* **114(4)**, 697–718.

Djon, M.L.N. & Barnes, S-J. (2012) Changes in sulfides and platinum-group minerals with the degree of alteration in the Roby, Twilight, and High Grade Zone of the Lac des Iles Complex, Ontario, Canada. *Mineralium Deposita* **47**, 875–896.

Docegeo - Rio Doce Geologia e Mineração (1988) Lithostratigraphic Review of the Carajás Mineral Province. SBG-NNO 35th Brazilian Geology Congress, Belém, Anais (11–59) (in Portuguese).

Duran, C.J., Barnes, S-J., & Corkery, J.T. (2015) Chalcophile and platinum-group element distribution in pyrites from the sulfide-rich pods of the Lac des Iles Pd deposits, Western Ontario, Canada: Implications for post-cumulus re-equilibration of the ore and the use of pyrite compositions in exploration. *Journal of Geochemical Exploration* **158**, 223–242.

Duran, C.J., Barnes, S-J., Pleše, P., Prašek, M.K., Zientek, M.L., & Pagé, P. (2017) Fractional crystallization-induced variations in sulfides from the Noril'sk-Talnakh mining district (polar Siberia, Russia). *Ore Geology Reviews* **90**, 326–351.

Duran, C.J., Dubé-Loubert, H., Pagé, P., Barnes, S-J., Roy, M., Savard, D., Cave, B., Arguin, J.P., & Mansur, E.T. (2019) Applications of trace element chemistry of pyrite and chalcopyrite in glacial sediments to mineral exploration targeting: Example from the Churchill Province, northern Quebec, Canada. *Journal of Geochemical Exploration* **196**, 105–130.

Ferreira Filho, C.F., Cançado, F., Correa, C., Macambira, E.M.B., Siepierski, L., & Brod, T.C.J. (2007) Stratiform EGP-Ni mineralizations associated with layered complexes in Carajás: the examples of Luanga and Serra da Onça. *Contributions to Amazon Geology* **5**, 1–14. (in Portuguese).

Figueiredo e Silva, R.C., Hagemann, S., Lobato, L.M., Rosiere, C.A., Banks, D.A., Davidson, G.J., & Hergt, J. (2013) Hydrothermal fluid processes and evolution of the giant Serra Norte jaspilite-hosted iron ore deposits, Carajás Mineral Province, Brazil. *Economic Geology* **108(4)**, 739–779.

Finnigan, C.S., Brenan, J.M., Mungall, J.E., & McDonough, W.F. (2008) Experiments and models bearing on the role of chromite as a collector of platinum group minerals by local reduction. *Journal of Petrology* **49**, 1647–1665.

Garcia, V.B., Schutesky, M.E., Oliveira, C.G., Whitehouse, M.J., Huhn, S.R., & Augustin, C.T. (2020) The Neoarchean GT-34 Ni deposit, Carajás Mineral Province, Brazil: an atypical IOCG-related Ni sulfide mineralization. *Ore Geology Reviews*, **127**.

George, L.L., Cook, N.J., Crowe, B. B., & Ciobanu, C.L. (2018) Trace elements in hydrothermal chalcopyrite. *Mineralogical Magazine* **82(1)**, 59–88.

Godel, B. & Barnes, S-J. (2008) Platinum-group elements in sulfide minerals and the whole rocks of the JM Reef (Stillwater Complex): Implication for the formation of the reef. *Chemical Geology* **248**, 272–294.

Godel, B., Barnes, S-J., & Maier, W.D. (2007) Platinum-group elements in sulphide minerals, platinum-group minerals, and whole-rocks of the Merensky Reef (Bushveld Complex, South Africa): Implications for the formation of the reef. *Journal of Petrology* **48**, 1569–1604.

Godel, B., González-Álvarez, I., Barnes, S.J., Barnes, S-J., Parker, P., & Day, J. (2012) Sulfides and sulfarsenides from the Rosie nickel prospect, Duketon greenstone belt, Western Australia. *Economic Geology* **107**, 275–294.

González-Álvarez, I., Pirajno, F., & Kerrich, R. (2013) Hydrothermal nickel deposits: Secular variation and diversity. *Ore Geology Reviews* **52**, 1–3.

González-Jiménez, J.M. & Reich, M. (2017) An overview of the platinum-group element nanoparticles in mantle-hosted chromite deposits. *Ore Geology Reviews* **81**, 1236–1248.

González-Jiménez, J.M., Deditius, A., Gervilla, F., Reich, M., Suvorova, A., Roberts, M.P., & Proenza, J.A. (2018) Nanoscale partitioning of Ru, Ir, and Pt in base-metal sulfides from the Caridad chromite deposit, Cuba. *American Mineralogist* **103(8)**, 1208–1220.

González-Jiménez, J.M., Roqué-Rosell, J., Jiménez-Franco, A., Tassara, S., Nieto, F., Gervilla, F., & Schilling, M. (2019) Magmatic platinum nanoparticles in metasomatic silicate glasses and sulfides from Patagonian mantle xenoliths. *Contributions to Mineralogy Petrology* **174(5)**, 47.

Grainger, C.J., Groves, D.I., Tallarico, F.H., & Fletcher, I.R. (2008) Metallogenesis of the Carajás mineral province, southern Amazon craton, Brazil: Varying styles of Archean through Paleoproterozoic to Neoproterozoic base-and precious-metal mineralisation. *Ore Geology Reviews* **33(3–4)**, 451–489.

Helmy, H.M. & Bragagni, A. (2017) Platinum-group elements fractionation by selective complexing, the Os, Ir, Ru, Rh-arsenide-sulfide systems above 1020°C. *Geochimica et Cosmochimica Acta* **216**, 169–183.

Helmy, H.M., Ballhaus, C., Berndt, J., Bockrath, C., & Wohlgemuth-Ueerwasser, C. (2007) Formation of Pt, Pd and Ni tellurides: Experiments in sulphide-telluride systems: *Contributions to Mineralogy and Petrology* **153**, 577–591.

Helmy, H.M., Ballhaus, C., Fonseca, R., & Nagel, T. (2013) Fractionation of platinum, palladium, nickel, and copper in sulfide–arsenide systems at magmatic temperature. *Contributions to Mineralogy and Petrology* **166**, 1725–1737.

Helmy, H.M., Ballhaus, C., Fonseca, R.O., & Leitzke, F.P. (2020) Concentrations of Pt, Pd, S, As, Se and Te in silicate melts at sulfide, arsenide, selenide and telluride saturation: evidence of PGE complexing in silicate melts?. *Contributions to Mineralogy and Petrology* **175(7)**, 1–14.

Hinchey, J.G. & Hattori, K.H. (2005) Magmatic mineralization and hydrothermal enrichment of the High Grade Zone at the Lac des Iles palladium mine, northern Ontario, Canada. *Mineralium Deposita* **40(1)**, 13–23.

Hoffman, E. & MacLean, W.H. (1976) Phase relations of michenerite and merenskyite in the Pd-Bi-Te system. *Economic Geology* **71**, 1461–1468.

Holwell, D.A. & Keays, R.R. (2014) The formation of low-volume, high-tenor magmatic PGE-Au sulfide mineralization in closed systems: evidence from precious and base metal geochemistry of the Platinova Reef, Skaergaard Intrusion, East Greenland. *Economic Geology* **109(2)**, 387–40.

Holwell, D. & McDonald, I. (2007) Distribution of platinum-group elements in the Platreef at Overysel, northern Bushveld Complex: A combined PGM and LA-ICP-MS study. *Contributions to Mineralogy and Petrology* **154**, 171–190.

Holwell, B.D. & McDonald, I. (2010) A review of the behaviour of platinum group elements within natural magmatic sulfide ore systems. *Platinum Metals Review* **54(1)**, 26–36.

Holwell, D., Adeyemi, Z., Ward, L.A., Smith, D.J., Graham, S.D., McDonald, I., & Smith, J.W. (2017) Low temperature alteration of magmatic Ni-Cu-PGE sulfides as a source for hydrothermal Ni and PGE ores: A quantitative approach using automated mineralogy. *Ore Geology Reviews* **91**, 718–740.

Holwell, D.A., Fiorentini, M., McDonald, I., Lu, Y., Giuliani, A., Smith, D.J., Keith, M., & Locmelis, M. (2019) A metasomatized lithospheric mantle control on the metallogenic signature of post-subduction magmatism. *Nature communications* **10(1)**, 1–10.

Hu, Z. & Gao, S. (2008) Upper crustal abundances of trace elements: a revision and update. *Chemical Geology* **253(3–4)**, 205–221.

Huang, X.W. & Beaudoin, G. (2019) Textures and chemical compositions of magnetite from iron oxide copper-gold (IOCG) and kiruna-type iron oxide-apatite (IOA) deposits and their implications for ore genesis and magnetite classification schemes. *Economic Geology* **114(5)**, 953–979.

Jenner, F.E. & O'Neill, H.S.C. (2012) Analysis of 60 elements in 616 ocean floor basaltic glasses. *Geochemistry, Geophysics, Geosystems* **13(2)**.

Jochum, K.P., Nohl, U., Herwig, K., Lammel, E., Stoll, B., & Hofmann, A.W. (2005) GeoReM: a new geochemical database for reference materials and isotopic standards. *Geostandards and Geoanalytical Research* **29(3)**, 333–338.

Junge, M., Wirth, R., Oberthür, T., Melcher, F., & Schreiber, A. (2015) Mineralogical siting of platinum-group elements in pentlandite from the Bushveld Complex, South Africa. *Mineralium Deposita* **50**, 41–54.

Junge, M., Oberthür, T., Kraemer, D., Melcher, F., Piña, R., Derrey, I.T., & Strauss, H. (2019) Distribution of platinum-group elements in pristine and near-surface oxidized Platreef ore and the variation along strike, northern Bushveld Complex, South Africa. *Mineralium Deposita* **54(6)**, 885–912.

Kamenetsky, V.S. & Zelenski, M. (2020) Origin of noble-metal nuggets in sulfide-saturated arc magmas: A case study of olivine-hosted sulfide melt inclusions from the Tolbachik volcano (Kamchatka, Russia). *Geology* **48(6)**, 620–624.

Kamenetsky, V.S., Park, J.W., Mungall, J.E., Pushkarev, E.V., Ivanov, A.V., Kamenetsky, M.B., & Yaxley, G.M. (2015) Crystallization of platinum-group minerals from silicate melts: Evidence from Cr-spinel–hosted inclusions in volcanic rocks. *Geology* **43(10)**, 903–906.

Kaukonen, R. (2008) Sulfide-poor platinum-group element deposits. Acta Unversitats Ouluensis, Oulu University Press, Finland.

Kawohl, A. & Frimmel, H.E. (2016) Isoferroplatinum-pyrrhotite-troilite intergrowth as evidence of desulfurization in the Merensky Reef at Rustenburg (western Bushveld Complex, South Africa). *Mineralogical Magazine* **80**, 1041–1053.

Ketris, M.P. & Yudovich, Y.E. (2009) Estimations of Clarkes for Carbonaceous biolithes: World averages for trace element contents in black shales and coals. *International Journal of Coal Geology* **78(2)**, 135–148.

Kitakaze, A., Machida, T., & Komatsu, R. (2016) Phase relations in the Fe-Ni-S system from 875 to 650°C. *The Canadian Mineralogist* **54**, 1175–1186.

Klein, C. & Ladeira, E.A. (2002) Petrography and geochemistry of the least altered banded iron-formation of the Archean Carajás Formation: Northern Brazil. *Economic Geology* **97**, 643–651.

Knight, R.D., Prichard, H.M., & Ferreira Filho, C.F. (2017) Evidence for As Contamination and the Partitioning of Pd into Pentlandite and Co + Platinum Group Elements into Pyrite in the Fazenda Mirabela Intrusion, Brazil. *Economic Geology* **112**, 1889–1912.

Knipping, J.L., Bilenker, L.D., Simon, A.C., Reich, M., Barra, F., Deditius, A.P., & Munizaga, R. (2015) Giant Kiruna-type deposits form by efficient flotation of magmatic magnetite suspensions. *Geology* **43(7)**, 591–594.

La Cruz, N.L., Ovalle, J.T., Simon, A.C., Konecke, B.A., Barra, F., Reich, M., & Childress, T.M. (2020) The geochemistry of magnetite and apatite from the El Laco iron oxide-apatite deposit, Chile: Implications for ore genesis. *Economic Geology* **115(7)**, 1461–1491.

Le Vaillant, M., Barnes, S.J., Fiorentini, M.L., Miller, J., McCuaig, T.C., & Muccilli, P. (2015) A hydrothermal Ni-As-PGE geochemical halo around the Miitel komatiite-hosted nickel sulfide deposit, Yilgarn Craton, Western Australia. *Economic Geology* **110(2)**, 505–530.

Le Vaillant, M., Saleem, A., Barnes, S.J., Fiorentini, M.L., Miller, J., Beresford, S., & Perring, C. (2016) Hydrothermal remobilisation around a deformed and remobilised komatiite-hosted Ni-Cu-(PGE) deposit, Sarah's Find, Agnew Wiluna greenstone belt, Yilgarn Craton, Western Australia. *Mineralium Deposita* **51(3)**, 369–388.

Le Vaillant, M., Barnes, S.J., Fiorentini, M.L., Barnes, S-J., Bath, A., & Miller, J. (2018) Platinum-group element and gold contents of arsenide and sulfarsenide minerals associated with Ni and Au deposits in Archean greenstone belts. *Mineralogical Magazine* **82(3)**, 625–647.

Lesher, C.M. & Burnham, O.M. (2001) Multicomponent elemental and isotopic mixing in Ni–Cu–(PGE) ores at Kambalda, Western Australia. *The Canadian Mineralogist* **39(2)**, 421–446.

Li, C., Ripley, E.M., Merino, E., & Maier, W.D. (2004) Replacement of base metal sulfides by actinolite, epidote, calcite, and magnetite in the UG2 and Merensky Reef of the Bushveld Complex: South Africa. *Economic Geology* **99**, 173–184.

Li, Y. & Audétat, A. (2015) Effects of temperature, silicate melt composition, and oxygen fugacity on the partitioning of V, Mn Co, Ni, Cu, Zn, As, Mo, Ag, Sn, Sb, W, Au, Pb, and Bi between sulfide phases and silicate melt. *Geochimica et Cosmochimica Acta* **162**, 25–45.

Liang, Q.L., Song, X.Y., Wirth, R., Chen, L.M., & Dai, Z.H. (2019) Implications of nano-and micrometer-size platinumgroup element minerals in base metal sulfides of the Yangliuping Ni-Cu-PGE sulfide deposit, SW China. *Chemical Geology* **517**, 7–21.

Liu, W., Migdisov, A., & Williams-Jones, A. (2012) The stability of aqueous nickel (II) chloride complexes in hydrothermal solutions: results of UV–visible spectroscopic experiments. *Geochimica et Cosmochimica Acta* **94**, 276–290.

Liu, Y. & Brenan, J. (2015) Partitioning of platinum-group elements (PGE) and chalcogens (Se, Te, As, Sb, Bi) between monosulfide-solid solution (MSS), intermediate solid solution (ISS) and sulfide liquid at controlled fO2–fS2 conditions. *Geochimica et Cosmochimica Acta* **159**, 139–161.

Lobato, L.M., Figueiredo e Silva, R.C., Rosière, C.A., Zucchetti, M., Baars, F.J., Seoane, J. C.S., Rios, F.J., & Monteiro, A.M. (2005) Hydrothermal origin for the iron mineralisation, Carajás Province, Pará State, Brazil. *In*

Proceedings Iron Ore 2005, The Australian Institute of Mining and Metallurgy, 99–110.

Lyubetskaya, T. & Korenaga, J. (2007) Chemical composition of Earth's primitive mantle and its variance: 1. Method and results. *Journal of Geophysical Research* **112(B3)**.

Maciag, B.J. & Brenan, J.M. (2020) Speciation of arsenic and antimony in basaltic magmas. *Geochimica et Cosmochimica Acta* **276**, 198–218.

Maier, W.D. (2005) Platinum-group element (PGE) deposits and occurrences: Mineralization styles, genetic concepts, and exploration criteria. *Journal of African Earth Sciences* **41**, 165–191.

Maier, W.D., Barnes, S-J., Gartz, V., & Andrews, G. (2003) Pt-Pd reefs in magnetitites of the Stella layered intrusion, South Africa: A world of new exploration opportunities for platinum group elements. *Geology* **31(10)**, 885–888.

Maier, W.D., Rasmussen, B., Fletcher, I., Godel, B., Barnes, S.J., Fisher, L., Yang, S.H., Huhma, H., & Lahaye, Y. (2015) Petrogenesis of the ~2.77 Ga Monts de Cristal Complex, Gabon: evidence for direct precipitation of Pt-arsenides from basaltic magma. *Journal of Petrology* **56**, 1285–1308.

Maier, W.D., Barnes, S-J., & Karykowski, B.T. (2016) A chilled margin of komatiite and Mg-rich basaltic andesite in the western Bushveld Complex, South Africa. *Contributions to Mineralogy and Petrology* **171(6)**, 57.

Mansur, E.T. & Barnes, S-J. (2020a) The role of Te, As, Bi, Sn and Sb during the formation of PGE deposits: examples from the Bushveld and Stillwater Complexes. *Geochimica et Cosmochimica Acta* **272**, 235–258.

Mansur, E.T. & Barnes, S.J. (2020b) Concentrations of Te, As, Bi, Sb and Se in the marginal zone of the Bushveld complex: Evidence for crustal contamination and the nature of the magma that formed the Merensky Reef. *Lithos*, 105407.

Mansur, E.T. & Ferreira Filho, C.F. (2016) Magmatic structure and geochemistry of the Luanga Mafic-Ultramafic Complex: further constraints for the PGE-mineralized magmatism in Carajás, Brazil. *Lithos* **266–267**, 28–43.

Mansur, E.T. & Ferreira Filho, C.F. (2017) Chromitites from the Luanga Complex, Carajás, Brazil: Stratigraphic distribution and clues to processes leading to post-magmatic alteration. *Ore Geology Reviews* **90**, 110–130.

Mansur, E.T., Barnes, S-J., & Duran, C.J. (2019) Textural and compositional evidence for the formation of pentlandite via peritectic reaction: Implications for the distribution of highly siderophile elements. *Geology* **47(4)**, 351–354.

Mansur, E.T., Barnes, S-J., & Duran, C.J. (2020a) Distribution of chalcophile and platinum-group elements among pyrrhotite, pentlandite, chalcopyrite and cubanite from the Noril'sk-Talnakh ores: Implications for the formation of platinum-group minerals. *Mineral Deposita* **55**, 1215–1232.

Mansur, E.T., Ferreira Filho, C.F., & Oliveira, D.P. (2020b) The Luanga deposit, Carajás Mineral Province, Brazil: Different styles of PGE mineralization hosted in a medium-size layered intrusion. *Ore Geology Reviews* **118**, 103340.

Mansur, E.T., Barnes, S-J., Savard, D., & Webb, P.C. (2020c) Determination of Te, As, Bi, Sb and Se (TABS) in Geological Reference Materials and GeoPT Proficiency Test Materials by Hydride Generation-Atomic Fluorescence Spectrometry (HG-AFS). *Geostandards and Geoanalytical Research* **44(1)**, 147–167.

Mansur, E.T., Barnes, S.J., & Duran, C.J. (2020d) An overview of chalcophile element contents of pyrrhotite, pentlandite, chalcopyrite, and pyrite from magmatic Ni-Cu-PGE sulfide deposits. *Mineralium Deposita*, 1–26.

McClenaghan, M.B. & Paulen, R.C. (2018) Application of till mineralogy and geochemistry to mineral exploration. *In* Past Glacial Environments, Second edition (J. Menzies & J. van der Meer, eds.). Elsevier (689–751).

McClenaghan, M.B., Averill, S.A., Kjarsgaard, I.M., Layton-Matthews, D., & Matile, G. (2011) Indicator mineral signatures of magmatic Ni-Cu deposits, Thompson Nickel Belt, central Canada. *In* Indicator Mineral Methods in Mineral Exploration (B. McClenaghan, V. Peuraniemi, & M. Lehtonen, eds.). Workshop in the 25th International Applied Geochemistry Symposium B92-4, 72.

McClenaghan, M.B., Ames, D.E., & Cabri, L.J. (2020) Indicator mineral and till geochemical signatures of the Broken Hammer Cu–Ni–PGE–Au deposit, North Range, Sudbury Structure, Ontario, Canada. *Geochemistry: Exploration, Environment, Analysis* **20(3)**, 337–356.

Molnár, F., Watkinson, D.H., & Jones, P.C. (2001) Multiple hydrothermal processes in footwall units of the North Range, Sudbury Igneous Complex, Canada, and implications for the genesis of vein-type Cu-Ni-PGE deposits. *Economic Geology* **96(7)**, 1645–1670.

Monteiro, L.V.S., Xavier, R.P., Hitzman, M.W., Juliani, C., de Souza Filho, C.R., & Carvalho, E.D.R. (2008) Mineral chemistry of ore and hydrothermal alteration at the Sossego iron oxide–copper–gold deposit, Carajás Mineral Province, Brazil. *Ore Geology Reviews* **34(3)**, 317–336.

Monteiro, L.V.S., Xavier, R.P., Souza Filho, C.R., & Moreto, C.P.N. (2014) Metallogenesis of the Carajás province. *Metallogenesis of Brazilian tectonic provinces*, 43–84. (in Portuguese).

Moreto, C.P.N., Monteiro, L.V., Xavier, R.P., Amaral, W.S., Dos Santos, T.J.S., Juliani, C., & de Souza Filho, C.R. (2011) Mesoarchean (3.0 and 2.86 Ga) host rocks of the iron oxide–Cu–Au Bacaba deposit, Carajás Mineral

Province: U–Pb geochronology and metallogenetic implications. *Mineralium Deposita* **46(7)**, 789.

Moreto, C.P., Monteiro, L.V., Xavier, R.P., Creaser, R.A., DuFrane, S.A., Melo, G. H., da Silva D., Marco, A., Tassinari, M.A., Colombo, C.G., & Sato, K. (2015) Timing of multiple hydrothermal events in the iron oxide–copper–gold deposits of the Southern Copper Belt, Carajás Province, Brazil. *Mineralium Deposita* **50(5)**, 517–546.

Mota-e-Silva, J., Prichard, H.M., Ferreira Filho, C.F., Fisher, P.C., & McDonald, I. (2015) Platinum-group minerals in the Limoeiro Ni–Cu–(PGE) sulfide deposit, Brazil: the effect of magmatic and upper amphibolite to granulite metamorphic processes on PGM formation. *Mineralium Deposita* **50(8)**, 1007–1029.

Mungall, J.E. & Brenan, J.M. (2014) Partitioning of platinum-group elements and Au between sulfide liquid and basalt and the origins of mantle-crust fractionation of the chalcophile elements. *Geochimica et Cosmochimica Acta* **125**, 265–289.

Mungall, J.E. & Naldrett, A.J. (2008) Ore deposits of the platinum-group elements. *Elements* **4**, 253–258.

Naldrett, A.J. (2004) Magmatic sulphide deposits: Geology, geochemistry and exploration. Springer-Verlag, Berlin, Germany.

Naldrett, A.J. (2010) Secular variation of magmatic sulfide deposits and their source magmas. *Economic Geology* **105(3)**, 669–688.

Oberthür, T., Melcher, F., Fusswinkel, T., van den Kerkhof, A.M., & Sosa, G.M. (2018) The hydrothermal Waterberg platinum deposit, Mookgophong (Naboomspruit), South Africa. Part 1: geochemistry and ore mineralogy. *Mineralogical Magazine* **82(3)**, 725–749.

Oliveira, M.M.F.D. (2017) Characterization and metallogenesis of the Jaguar Ni deposit, Carajás Mineral Province. Unpublished M.Sc. thesis, Universidade de Brasília, Brasília, Brazil. (in Portuguese).

Oppermann, L., Junge, M., Schuth, S., Holtz, F., Schwarz-Schampera, U., & Sauheitl, L. (2017) Mobility and distribution of palladium and platinum in soils above Lower and Middle Group chromitites of the western Bushveld Complex, South Africa. *South African Journal of Geology* **120(4)**, 511–524.

Osbahr, I., Oberthür, T., Klemd, R., & Josties, A. (2014) Platinum-group element distribution in base-metal sulfides of the UG2 chromitite, Bushveld Complex, South Africa - a reconnaissance study. *Mineralium Deposita* **49(6)**, 655–665.

Paton, C., Hellstrom, J., Paul, B., Woodhead, J., & Hergt, J. (2011) Iolite: freeware for the visualisation and processing of mass spectrometric data. *Journal of Analytical Atomic Spectrometry* **26**, 2508–2518.

Patten, C., Barnes, S-J., Mathez, E.A., & Jenner, F.E. (2013) Partition coefficients of chalcophile elements between sulfide and silicate melts and the early crystallization history of sulfide liquid: LA-ICP-MS analysis of MORB sulfide droplets. *Chemical Geology* **358**, 170–188.

Patten, C.G., Pitcairn, I.K., Teagle, D.A., & Harris, M. (2016). Mobility of Au and related elements during the hydrothermal alteration of the oceanic crust: implications for the sources of metals in VMS deposits. *Mineralium Deposita* **51(2)**, 179–200.

Patten, C.G., Pitcairn, I.K., & Teagle, D.A.H. (2017) Hydrothermal mobilisation of Au and other metals in supra-subduction oceanic crust: Insights from the Troodos ophiolite. *Ore Geology Reviews* **86**, 487–508.

Péntek, A., Molnár, F., Watkinson, D.H., & Jones, P.C. (2008) Footwall-type Cu-Ni-PGE Mineralization in the Broken Hammer Area, Wisner Township, North Range, Sudbury Structure. *Economic Geology* **103(5)**, 1005–1028.

Pestilho, A.L.S., Monteiro, L.V.S., de Melo, G.H.C., Moreto, C.P.N., Juliani, C., Fallick, A.E., & Xavier, R.P. (2020) Stable isotopes and fluid inclusion constraints on the fluid evolution in the Bacaba and Castanha iron oxide-copper-gold deposits, Carajás Mineral Province, Brazil. *Ore Geology Reviews*, 103738.

Piña, R., Gervilla, F., Barnes, S-J., Ortega, L., & Lunar, R. (2012) Distribution of platinum-group and chalcophile elements in the aguablanca Ni-Cu sulfide deposit (SW Spain): Evidence from a LA-ICP-MS study. *Chemical Geology* **302**, 61–75.

Piña, R., Gervilla, F., Barnes, S-J., Ortega, L., & Lunar, R. (2015) Liquid immiscibility between arsenide and sulfide melts: evidence from a LA-ICP-MS study in magmatic deposits at Serranía de Ronda (Spain). *Mineralium Deposita* **50(3)**, 265–279.

Piña, R., Gervilla, F., Barnes, S-J., Oberthür, T., & Lunar, R. (2016) Platinum-group element concentrations in pyrite from the Main Sulfide Zone of the Great Dyke of Zimbabwe. *Mineralium Deposita* **51(7)**, 853–872.

Polovina, J.S., Hudson, D.M., & Jones, R.E. (2004) Petrographic and geochemical characteristics of post-magmatic hydrothermal alteration and mineralization in the J-M Reef, Stillwater Complex, Montana. *The Canadian Mineralogist* **42**, 261–278.

Queffurus, M. & Barnes, S-J. (2015) A review of sulfur to selenium ratios in magmatic nickel–copper and platinum-group element deposits. *Ore Geology Reviews* **69**, 301–324.

Rosa, W.D. (2014) Serra da Onça and Serra do Puma bedded complexes: Geology and petrology of two Mafic-Ultramafic intrusions with distinct crystallization sequence in the Archean Province of Carajás, Brazil. Unpublished M.Sc. thesis, Universidade de Brasília, Brasília, Brazil. (in Portuguese).

Samalens, N., Barnes, S-J., & Sawyer, E.W. (2017a) A laser ablation inductively coupled plasma mass spectrometry

study of the distribution of chalcophile elements among sulfide phases in sedimentary and magmatic rocks of the Duluth Complex, Minnesota, USA. *Ore Geology Reviews* **90**, 352–370.

Samalens, N., Barnes, S-J., & Sawyer, E.W. (2017b) The role of black shales as a source of sulfur and semimetals in magmatic nickel-copper deposits: Example from the Partridge River Intrusion, Duluth Complex, Minnesota, USA. *Ore Geology Reviews* **81(1)**, 173–187.

Savard, D., Barnes, S.J., & Meisel, T. (2010) Comparison between nickel-sulfur fire assay Te co-precipitation and isotope dilution with high-pressure asher acid digestion for the determination of platinum-group elements, rhenium and gold. *Geostandards and Geoanalytical Research* **34(3)**, 281–291.

Scholten, L., Watenphul, A., Beermann, O., Testemale, D., Ames, D., & Schmidt, C. (2018) Nickel and platinum in high-temperature H_2O+HCl fluids: implications for hydro- thermal mobilization. *Geochimica et Cosmochimica Acta* **224**, 187–199.

Schutesky, M.E. & de Oliveira, C.G. (2020) From the roots to the roof: an integrated model for the Neoarchean Carajás IOCG System, Brazil. *Ore Geology Reviews*, 103833.

Siepierski, L. & Ferreira Filho, C.F. (2020) Magmatic structure and petrology of the Vermelho Complex, Carajás Mineral Province, Brazil: Evidence for magmatic processes at the lower portion of a mafic-ultramafic intrusion. *Journal of South American Earth Sciences* **102**, 102700.

Simon, A.C., Knipping, J., Reich, M., Barra, F., Deditius, A.P., Bilenker, L., & Childress, T. (2018) Kiruna-type iron oxide-apatite (IOA) and iron oxide copper-gold (IOCG) deposits form by a combination of igneous and magmatic-hydrothermal processes: Evidence from the Chilean iron belt. *Society of Economic Geologists Special Publication* **21**, 89–114.

Sluzhenikin, S.F., Krivolutskaya, N.A., Rad'ko, V.A., Malitch, K.N., Distler, V.V., & Fedorenko, V.A. (2014) Ultramafic-mafic intrusions, volcanic rocks and PGE-Cu-Ni sulfide deposits of the Noril'sk Province, Polar Siberia. Field trip guidebook.

Sluzhenikin, S.F., Yudovskaya, M.A., Barnes, S.J., Abramova, V.D., Le Vaillant, M., Petrenko, D.B., & Brovchenko, V.D. (2020) Low-sulfide platinum group element ores of the Norilsk-Talnakh camp. *Economic Geology* **115(6)**, 1267–1303.

Tanner, D., McDonald, I., Harmer, R.J., Muir, D.D., & Hughes, H.S. (2019) A record of assimilation preserved by exotic minerals in the lowermost platinum-group element deposit of the Bushveld Complex: The Volspruit Sulphide Zone. *Lithos* **324**, 584–608.

Tao, Y., Li, C., Hu, R., Ripley, E.M., Du, A., & Zhong, H. (2007) Petrogenesis of the Pt–Pd mineralized Jinbaoshan ultramafic intrusion in the Permian Emeishan large igneous province, SW China. *Contributions to Mineralogy and Petrology* **153(3)**, 321–337.

Tavares, F.M., Trouw, R.A.J., da Silva, C.M.G., Justo, A.P., & Oliveira, J.K.M. (2018) The multistage tectonic evolution of the northeastern Carajás Province, Amazonian Craton, Brazil: Revealing complex structural patterns. *Journal of South American Earth Sciences* **88**, 238–252.

Teixeira, A.S., Ferreira Filho, C.F., Giustina, M.E.S.D., Araujo, S.M., & Silva, H.H.A.B. (2015) Geology, petrology and geochronology of the Lago Grande layered complex: evidence for a PGE-mineralized magmatic suite in the Carajás Mineral Province, Brazil. *Journal of South American Earth Sciences* **64**, 116–138.

Tian, Y., Etschmann, B., Liu, W., Borg, S., Mei, Y., Testemale, D., O'Neill, B., Rae, N., Sherma, D.M., Ngothai, Y., Johannessen, B., Glover, C., & Brugger, J. (2012) Speciation of nickel (II) chloride complexes in hydrothermal fluids: in situ XAS study. *Chemical Geology* **334**, 345–363.

Tomkins, A.G., Pattison, D.R.M., & Frost, B.R. (2007) On the initiation of metamorphic sulphide anatexis. *Journal of Petrology* **48**, 511–535.

Torresi, I., Xavier, R.P., Bortholoto, D.F., & Monteiro, L.V. (2012) Hydrothermal alteration, fluid inclusions and stable isotope systematics of the Alvo 118 iron oxide–copper–gold deposit, Carajás Mineral Province (Brazil): implications for ore genesis. *Mineralium Deposita* **47(3)**, 299–323.

Tredoux, M., Lindsay, N.M., Davies, G., & McDonald, I. (1995) The fractionation of platinum group elements in magmatic systems, with the suggestion of a novel causal mechanism. *South African Journal of Geology* **98**, 157–167.

Tuba, G., Molnár, F., Ames, D.E., Péntek, A., Watkinson, D.H., & Jones, P.C. (2014) Multistage hydrothermal processes involved in "low-sulfide" Cu (-Ni)-PGE mineralization in the footwall of the Sudbury Igneous Complex (Canada): Amy Lake PGE zone East Range. *Mineralium Deposita* **49**, 7–47.

van den Kerkhof, A.M., Sosa, G.M., Oberthür, T., Melcher, F., Fusswinkel, T., Kronz, A., & Dunkl, I. (2018) The hydrothermal Waterberg platinum deposit, Mookgophong (Naboomspruit), South Africa Part II: Quartz chemistry, fluid inclusions and geochronology. *Mineralogical Magazine* **82(3)**, 751–778.

Vasquez, M.L., Carvalho, J.M.A., Sousa, C.S., Ricci, P.S.F., Macambira, E.M.B., & Costa, L.T.R. (2008) Geological map of the Pará state in GIS, Geological Survey of Brazil-CPRM.

Veloso, A.S.R., Monteiro, L.V.S., & Juliani, C. (2020) The link between hydrothermal nickel mineralization and an iron oxide-copper-gold (IOCG) system: constraints based on mineral chemistry in the Jatobá deposit, Carajás Province. *Ore Geology Reviews*, 103555.

Wang, C.Y., Prichard, H.M., Zhou, M.F., & Fisher, P.C. (2008) Platinum-group minerals from the Jinbaoshan Pd–Pt deposit, SW China: evidence for magmatic origin and hydrothermal alteration. *Mineralium Deposita* **43(7)**, 791.

Wilson, A.H. (2012) A chill sequence to the Bushveld Complex: insight into the first stage of emplacement and implications for the parental magmas. *Journal of Petrology* **53(6)**, 1123–1168.

Wirth, R., Reid, D., & Schreiber, A. (2013) Nanometer-sized platinum-group minerals (PGM) in base metal sulfides: new evidence for an orthomagmatic origin of the Merensky Reef PGE ore deposit, Bushveld Complex, South Africa. *The Canadian Mineralogist* **51**, 143–155.

Wood, S.A. (2002) The aqueous geochemistry of the platinum group elements with applications to ore deposits. *In* Geology, Geochemistry, Mineralogy and Mineral Benefication of Platinum Group Element. *Canadian Institute of Mining, Metallurgy and Petroleum, Special volume* **54**, 211–249.

Xavier, R.P., Wiedenbeck, M., Trumbull, R.B., Dreher, A.M., Monteiro, L.V., Rhede, D., & Torresi, I. (2008) Tourmaline B-isotopes fingerprint marine evaporites as the source of high-salinity ore fluids in iron oxide copper-gold deposits, Carajás Mineral Province (Brazil). *Geology* **36(9)**, 743–746.

Xavier, R., Monteiro, L.V.S., Souza Filho, C.R., Torresi, I., Carvalho, E.R., Dreher, A.M., Wiedenbeck, M., Trumbull, R.B., Pestilho, A.L.S., & Moreto, C.P.N. (2010) The iron oxide copper-gold deposits of the Carajás Mineral Province, Brazil: an updated and critical review. *In* Hydrothermal Iron Oxide Copper-Gold & Related Deposits: A Global Perspective, Advances in the Understanding of IOCG Deposits (T.M. Porter, ed.). Linden Park, Adelaide, Australia (285–306).

Xavier, R.P., Monteiro, L.S., Moreto, C.P.N., Pestilho, A.L.S., Melo, G.D., Silva, M.D., Aires, B., Ribeiro, C., & Silva, F.E. (2012) The iron oxide copper-gold systems of the Carajás mineral province, Brazil. *Society of Economic Geologists* **16**, 433–453.

Received February 18, 2021. Revised manuscript accepted June 15, 2021.